

Secondary flow-induced particle dynamics in fully developed turbulent square ducts with a free-slip boundary

Yanzhi Wang^{a*}, Wenli Ma^a, Lee F. Mortimer^b, Michael Fairweather^b, Shuai Wang^a

^a*Yan'an Engineering Technology Research Centre of Efficient Pipeline Transportation of Oil and Gas and Flow Guarantee, School of Petroleum Engineering and Environmental Engineering, Yan'an University, Yan'an 716000, China*

^b*School of Chemical and Process Engineering, University of Leeds, Leeds, LS2 9JT, UK*

*Corresponding author at: Yan'an Engineering Technology Research Centre of Efficient Pipeline Transportation of Oil and Gas and Flow Guarantee, School of Petroleum Engineering and Environmental Engineering, Yan'an University, Yan'an 716000, Shaanxi, China.

Telephone: +86-0911-2650332; E-mail address: yanzhiwang@yau.edu.cn

ABSTRACT

Secondary flow effects on particle dynamics are investigated in a fully developed turbulent open square duct flow at a shear Reynolds number of $Re_\tau=300$. The modelling of the fluid phase is based on direct numerical simulation, and the trajectories of particles are described using a one-way coupled Lagrangian particle tracking technique, with shear Stokes numbers ranging from $St^+=0.31\sim 260$. The results obtained show that particles with $St^+\geq 25$ accumulate strongly in the lower corners of the duct, while the upper corners with mixed boundaries are relatively devoid of particles. The transverse cross-stream velocities for all considered particle sets exceed those of the fluid phase near the intersection of the inner and outer secondary vortices. Furthermore, the cross-sectional secondary flow is observed to encourage particle acceleration near the free surface. A further in-depth analysis regarding the impact of various hydrodynamic forces exerted on the particles in the duct cross-section is also provided.

Key words: Particle dynamics, Turbulence, Secondary flow, Open duct, Direct numerical simulation

1. Introduction

Particle transport in turbulent wall-bound flows has significant relevance in many engineering and environmental processes, including pneumatic conveying [1], ventilation and air-conditioning systems [2], heat exchangers [3] as well as petroleum and chemical reactors [4]. To understand the underlying mechanisms behind how particles are transported in such flows, numerous experimental and numerical studies have been conducted to investigate particle behavior in canonical turbulent channel flows and wall boundary layers [5-8]. However, most industrial applications often involve internal flows with complex, non-canonical geometries where the secondary flows may occur, which further leads to more complicated particle behavior [9-12]. Therefore, gaining a thorough understanding of particle dynamics in such flows is crucial for improving and optimizing related engineering equipment and processes.

In the present study, attention is focused on turbulent straight duct flows, where the secondary flow is induced by the turbulence anisotropy. The behavior of inertial particles in such flows has been extensively studied. Phares and Sharma [13] conducted the first direct numerical simulation of a turbulent particle-laden flow in a horizontal square duct. They observed that the off-axis secondary flow can enhance the accumulation of high-inertia particles near the corners of the duct, while inhibiting the deposition of low-inertia particles in this region. Winkler et al. [14] studied a similar phenomenon in a vertically downward square duct flow and found that low-inertia particles are more prone to deposit near the center of the duct walls, with a higher deposition rate than that in circular pipe flows where the secondary flow is absent. Fairweather and Yao [15, 16] extended these investigations to higher Reynolds numbers, with their findings confirming the observations made by the two research groups mentioned above. Later, Noorani et al. [17] further analyzed the Eulerian statistics of Lagrangian particles in turbulent duct flows by varying the aspect ratio of the duct. Their results demonstrated that the cross-stream secondary motions have a significant impact on the cross-stream particle concentration distribution, and particle mean and fluctuating velocities. In addition, the correlation between particle distribution and near-wall turbulent structures in turbulent square duct flows was studied by Wang et al. [18] who demonstrated that particle accumulation in the corners of the duct is dominated by the secondary flows, while in the central regions of the duct walls particle accumulation is mainly dependent on the near-wall coherent vortices.

In terms of particle dynamics, previous numerical studies of turbulent particle-laden channel flows based on the point-particle approximation typically take the drag force into consideration, while selectively ignoring other forces due to their differing research aims. In such flows, the shear-induced lift force is generally small compared to the

drag force, but becomes more important near the wall for high-inertia particles [19, 20]. Additionally, its inclusion can lead to a weakened near-wall particle accumulation in channel flows [21-23]. The pressure gradient force was also demonstrated to be relevant near the wall, with its effect on particle motion being appreciable when the two-phase density ratio is close to unity. As for the added mass force, it can be generally be neglected [24, 25]. In contrast, the presence of secondary flows in turbulent ducts can alter the distribution of flow velocities and their gradients in the duct cross-section, which can potentially affect the hydrodynamic forces acting on the particles. Winkler and Rani [26] first pointed out that particles in turbulent square duct flows experience a net mean cross-sectional drag force towards the duct corners. They also emphasized that shear-induced lift forces due to secondary flow velocity gradients are not as significant as those arising from streamwise velocity gradients. Yao and Fairweather [27] found that the drag force induced by the secondary flows can promote particle re-suspension along the wall-normal direction within the duct cross-section, with this effect more pronounced for smaller particles. While the influence of the lift force varies depending on the direction of the secondary flows, it becomes increasingly significant as particle size increases and when particles are near the duct wall. In a recent study, Wang et al. [18] provided a comprehensive analysis of the impact of different forces on particle motion in the cross-section of a square duct flow. They revealed that the cross-sectional average drag force, pressure gradient force and added mass force all contribute to driving high-inertia particles away from the duct walls in the near-wall region, whereas the lift force tends to push particles toward the corners and walls of the duct, with its effect more significant in the viscous sublayer as the particle Stokes number increases. Furthermore, pressure gradient forces were also shown to play a significant role in governing the cross-sectional motions of low-inertia particles.

It should be noted that the particle-laden duct flow studies cited above all pertain to closed ducts with no-slip boundaries. However, when a solid boundary changes to a free surface or a free-slip wall, as in typical environmental processes such as sediment transport in narrow rivers, there will be substantial changes in the strength and topology of the secondary flows in the cross-section of the duct [28-30]. A distinctive feature of turbulent open duct flows is the presence of inner and outer secondary vortices near the corners of the open duct, characterized by mixed boundaries involving both solid walls and a free surface. Moreover, the maximum intensity of the secondary flows in open ducts is observed to be higher than that found in closed ducts [29]. These differences from closed duct flows are anticipated to cause different particle behavior in turbulent open duct flow scenarios. Nevertheless, research on particle-laden flows in open ducts remains relatively limited. Kundu and Ghoshal [31] initially identified that secondary flows play an important role in the concentration distribution of sediment in open channel flows. Wang et

al. [32] observed that particle dispersion in turbulent open duct flows is inhibited compared to closed duct flows at the same Reynolds number, with this trend becoming more pronounced with increasing particle size and Stokes number. Recently, they further established that particle concentration near the side walls is lower than that near the bottom wall due to the convection effects of the secondary flows in these systems. In addition, the minimum particle concentration is achieved at the free surface, whilst heavier particles tend to concentrate preferentially in regions characterized by negative instantaneous transverse cross-stream velocities [33]. Given the limited number of studies, there remains a paucity of research focused on particle dynamics induced by secondary flows adjacent to mixed boundaries in open ducts. Furthermore, the dependence of these dynamics on a wide range of relevant Stokes numbers has yet to be thoroughly elucidated.

Therefore, this study aims to elaborate the particle dynamics induced by secondary flows in turbulent ducts with a free-slip boundary (hereinafter referred to as open ducts) through direct numerical simulations combined with a one-way coupled Lagrangian particle tracking technique. The flow shear Reynolds number, based on the duct half-height and mean friction velocity, is set at $Re_\tau=300$. Four different particle-fluid density ratios are analyzed, corresponding to shear Stokes numbers of $St^+=0.31, 25, 125$ and 260 . The paper is organized as follows: Section 2 describes the flow configuration and numerical methods used for both the fluid and particulate phases, followed by a brief validation of the single-phase flow. In Section 3, the instantaneous spatial distribution of particles as well as their mean Euler statistics relating to concentration, velocities, accelerations and dynamics across the cross-section of the open duct are discussed in detail. Finally, the conclusions are summarized in Section 4.

2. Methodology

2.1. Flow configuration

The configuration of the current open square duct flow is shown in Fig. 1. The origin of the Cartesian coordinate system is situated at the center of the duct, with the streamwise flow direction aligned with the x -axis, and the transverse and spanwise directions along y - and z - axes, respectively. The half-height of the duct is represented as h , and the dimensions of the square domain are $[-4\pi h, 4\pi h] \times [-h, h] \times [-h, h]$ in the x, y, z directions. The corresponding velocity components in the (x, y, z) directions are denoted as (u, v, w) . Periodic boundary conditions are enforced in the streamwise direction, while no-slip boundary conditions are applied to both side and bottom walls of the duct. Since the flow Froude number considered in this study is relatively low, the deformation of the free surface can be negligible [34]. Furthermore, previous research has demonstrated that small deformations of the free

surface have a minimal impact on turbulence structure in open channel flows [35]. Therefore, no-stress or free-slip boundary conditions are enforced at the upper surface of the computational domain:

$$\frac{\partial u}{\partial y} = \frac{\partial w}{\partial y} = v = 0 \quad (1)$$

In the present study, the duct half-height h is considered as the characteristic length, and either the bulk velocity u_b or friction velocity u_τ is chosen as the characteristic velocity for use in making related physical quantities dimensionless. The bulk Reynolds number, defined as $Re_b = u_b h / \nu$, is set at 5010, with a corresponding shear Reynolds number, $Re_\tau = u_\tau h / \nu$, of 300. Here, ν represents the kinematic viscosity of the fluid, and mean friction velocity is given as $u_\tau = \sqrt{\bar{\tau}_w / \rho_f}$, where $\bar{\tau}_w$ denotes the average shear stress over the three duct walls, and ρ_f is the fluid density. Normalization to the viscous scales based on the friction velocity or viscous length is denoted by the superscript “+”, i.e., $u^+ = u / u_\tau$, $x^+ = x u_\tau / \nu$, and $t^+ = t u_\tau^2 / \nu$, while that to the integral scales based on the bulk velocity or characteristic length is denoted by the superscript “*”, i.e., $u^* = u / u_b$, $x^* = x / h$, and $t^* = t u_b / h$, respectively.

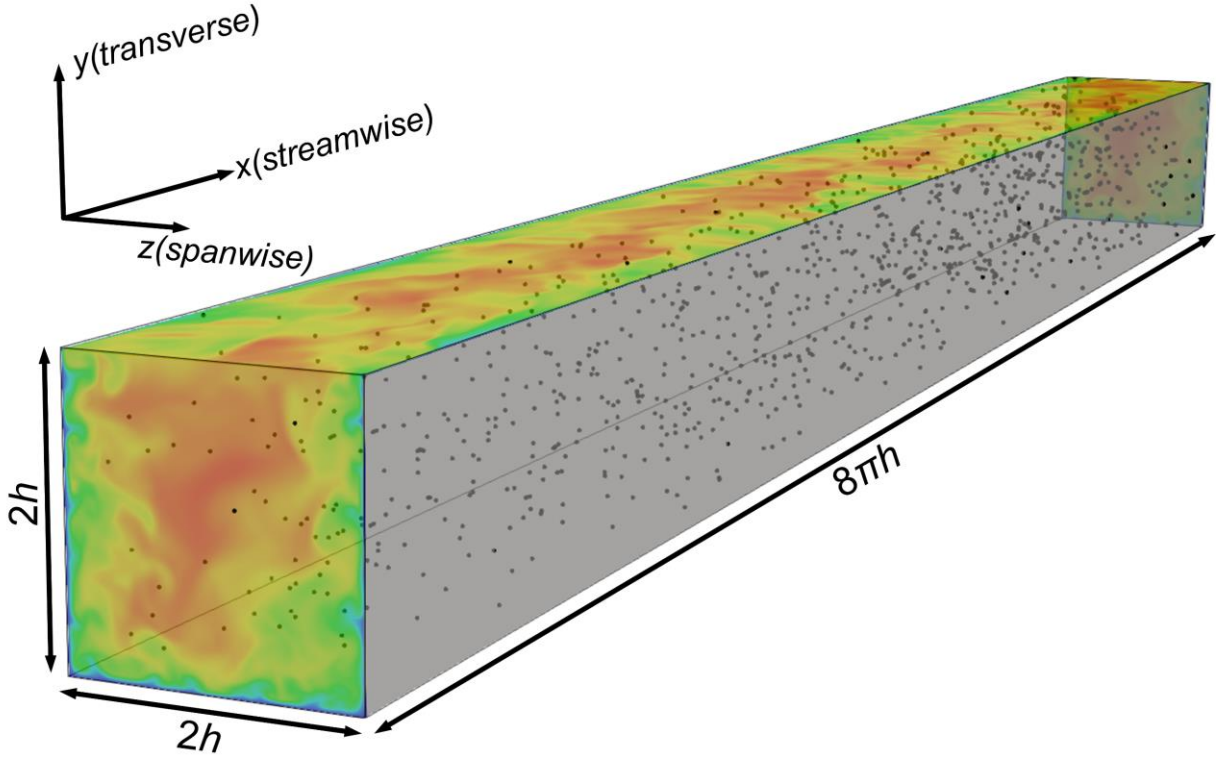


Fig. 1. Instantaneous snapshot of the fluid streamwise velocity together with solid particle locations in an open square duct flow.

2.2. Numerical simulation for the fluid phase

Direct numerical simulation (DNS), conducted with the Nek5000 code [36] based on the spectral-element method (SEM) [37], was employed to solve the problem of three-dimensional incompressible flows in the present open square duct. The corresponding Navier–Stokes equations are non-dimensionalized based on the integral scales:

$$\nabla \cdot \mathbf{u}^* = 0 \quad (2)$$

$$\frac{\partial \mathbf{u}^*}{\partial t^*} + \mathbf{u}^* \cdot \nabla \mathbf{u}^* = -\nabla p^* + \frac{1}{Re_b} \nabla \cdot \boldsymbol{\tau}^* + \mathbf{f}^* \quad (3)$$

where \mathbf{u}^* represents the fluid velocity, p^* denotes fluid pressure, $\boldsymbol{\tau}^*$ is the stress tensor, and \mathbf{f}^* is an additional source term which accounts for acceleration exerted in the streamwise direction to maintain a constant mass flow rate throughout the entire duct.

Based on the SEM [37], the current square domain is decomposed into $48 \times 24 \times 24$ spectral elements. The nodes of these elements are distributed uniformly in the streamwise direction and clustered towards the solid walls or free surface in the transverse or spanwise directions. Inside each element, the fluid velocities are solved at the Gauss-Lobatto-Legendre points using 8th order Lagrange interpolants, with pressure solved at two orders lower. This results in grid point spacing ranging from $\Delta x^+ = 10.05$ – 30.65 in the x direction, and from $\Delta y^+ (\Delta z^+) = 0.38$ – 12.3 in the $y(z)$ directions. The fluid solver time step is set to be $\Delta t^+ = 0.002$, which is sufficiently small to ensure that the flow Courant-Friedrichs-Lewy number remains below 0.5 throughout the simulation. The Nek5000 code has been previously used to successfully predict the turbulent flow dynamics in channels [25], ducts [17] and pipes [38]. Its high-order accuracy and reliability have been widely tested and validated. More information about the code and grid parameters of the specific duct domain used in this study can be found in our previous works [18, 33].

2.3. Modelling of the particulate phase

For the particulate phase, a point-source Lagrangian particle tracking (LPT) approach is utilized to model particle motion in the fully developed flow field. This approach assumes that the particle size is smaller than the flow Kolmogorov scale η_κ . Bagchi and Balachandar [39] reported that turbulence effects on the drag and lift forces acting on particles can be accurately predicted when the particle diameter falls within the range of $1.5\eta_\kappa < d_p < 10\eta_\kappa$. Based on the time- and space-averaged dissipation rate of the present flow, the particle diameter chosen in this study ranged from $2.9\eta_\kappa < d_p < 8.1\eta_\kappa$, and the particles are assumed to be rigid spheres with identical diameters and densities. Furthermore, the particle volume fraction ($\phi_V \leq 10^{-4}$) is set sufficiently low so that particle-induced effects

on the flow or inter-particle collisions can be neglected, which is known as the one-way coupling. The forces considered acting on the particles include the drag, lift, added mass and pressure gradient forces, thus the dimensionless equations of motion of individual particle can be written as:

$$\frac{d\mathbf{u}_p^*}{dt^*} = \underbrace{\frac{3C_D|\mathbf{u}_s^*}{4d_p^*\rho_p^*}\mathbf{u}_s^*}_{\text{Drag force}} + \underbrace{\frac{3C_L}{4\rho_p^*}(\mathbf{u}_s^* \times \boldsymbol{\omega}^*)}_{\text{Shear lift force}} + \underbrace{\frac{C_{am}}{\rho_p^*}\left(\frac{D\mathbf{u}^*}{Dt^*} - \frac{d\mathbf{u}_p^*}{dt^*}\right)}_{\text{Added mass force}} + \underbrace{\frac{1}{\rho_p^*}\frac{D\mathbf{u}^*}{Dt^*}}_{\text{Pressure gradient force}} \quad (4)$$

$$\frac{d\mathbf{x}_p^*}{dt^*} = \mathbf{u}_p^* \quad (5)$$

where the terms on the right-hand side of Eq. (4) represent the contributions to particle acceleration from the drag force, shear-lift force, added mass force and pressure gradient force, respectively. \mathbf{x}_p^* is the particle position, \mathbf{u}_p^* is the particle velocity, ρ_p^* is the two-phase density ratio, d_p^* is the particle diameter, $\boldsymbol{\omega}^* = \nabla \times \mathbf{u}^*$ is the fluid curl and $\mathbf{u}_s^* = \mathbf{u}^* - \mathbf{u}_p^*$ is the relative slip velocity at the particle location. $D\mathbf{u}^*/Dt^*$ is the material derivative of the fluid velocity, which is calculated instantaneously at the particle location using the spectral interpolation algorithm in Nek5000. C_D is the coefficient of Stokes drag and C_L the coefficient of shear-induced lift. The expressions used for C_D and C_L can be found in the literature [40], where near-wall effects on the drag and lift forces were also included. C_{am} is the coefficient for the added mass force, and its value is 0.5 for spherical particles [41]. Regarding the Basset force, Armenio and Fiorotto [24] reported that its impact on particle dispersion diminishes as particle inertia increases. The ratio of its average value to that of the drag force ranges from 0.25 to 0.095 when the two-phase density ratio changes between 2.65 and 2650. However, due to its high demand for computational resources, the Basset force is not considered in this study. In addition, gravity and buoyancy are also neglected in order to isolate secondary flow effects on particle dynamics.

The fourth-order Runge–Kutta scheme was used to solve the particle equation of motion. The integration time step is set to match that of the flow solver. Initially, particles were randomly distributed throughout the duct, with their initial velocity set to be the local fluid velocity at their location, which was achieved using the high accuracy spectral interpolation algorithm provided in Nek5000. In the streamwise direction, particles leaving the duct would re-enter the domain by applying periodic boundary conditions for both particle position and velocity. The top free-slip boundary is assumed to be completely absorbing, meaning that a particle will be removed from the computational domain if it comes within one particle radius of the free surface. Particle-wall collisions are considered fully elastic. To maintain a constant total number of particles, a new random particle is introduced into the domain whenever a particle touches the free-slip boundary. The present LPT code has been previously verified and validated for particle-laden turbulent channel and closed duct flows in studies by Mortimer et al. [25] and Wang et al. [18].

Table 1 Simulation parameters for the particulate phase.

Parameter		$St^+=0.31$	$St^+=25$	$St^+=125$	$St^+=260$
Number of particles	N_p	100,000	100,000	100,000	100,000
Particle diameter	d_p^*	0.005	0.005	0.005	0.005
	d_p^+	1.5	1.5	1.5	1.5
Particle and fluid time step	Δt^*	0.002	0.002	0.002	0.002
	Δt^+	0.036	0.036	0.036	0.036
Particle volume fraction	ϕ_V	10^{-4}	10^{-4}	10^{-4}	10^{-4}
Bulk Stokes number	St_b	0.017	1.39	6.96	14.45
Shear Stokes number	St^+	0.31	25.0	125.0	259.5
Density ratio	ρ_p^*	2.5	200	1000	2076

In this study, four particle Stokes numbers are investigated, with density ratios ranging from 2.5 to 2076. For each particle Stokes number, 100,000 particles were tracked along their trajectories. Two types of Stokes numbers are used to evaluate the significance of particle inertia. The first is the dimensionless bulk Stokes number $St_b = Re_b d_p^{*2} \rho_p^* / 18$, which represents the particle relaxation time normalized by the integral scale. The second is the shear Stokes number $St^+ = Re_\tau^2 d_p^{*2} \rho_p^* / 18$, which is non-dimensionalized by the viscous scale. The bulk Stokes numbers considered in this work range from $St_b=0.017$ to 14.45, with the corresponding shear Stokes number varying from $St^+=0.31$ to 259.5. The simulation parameters for the particulate phase are summarized in Table 1.

2.4. Flow field validation

The flow field was initialized using a fully developed turbulent channel flow at the present Reynolds number. The Navier-Stokes equations were then integrated until a statistically steady state was achieved. The attainment of this steady state was determined by closely monitoring the mean streamwise velocity, the root mean square (*r.m.s.*) of velocity fluctuations, and the mean shear stress along the bottom wall centerline. Subsequently, data on flow statistics were collected for an additional 1500 integral time units. Based on these data, mean flow statistics were obtained by applying time averaging and spatial averaging in the streamwise direction, as well as across the bottom wall symmetry plane.

Fig. 2(a) shows contours of the instantaneous streamwise velocity in the cross-sectional plane of the open duct, with superimposed cross-stream secondary flow velocity vectors in the right-hand panel. It is evident that the near-wall turbulent structures associated with ejection and sweep events are well resolved. The typical mushroom-shaped

coherent structures, which are linked to the generation of turbulence-driven secondary flows [42], are clearly observed in the lower corners of the open duct. The left-half panel of Fig. 2(b) presents the distribution of the mean flow streamwise velocity. It is worth noting that the position of maximum streamwise velocity is located beneath the free surface, which is referred to as the velocity-dip phenomenon in rectangular open channel flows [43]. Furthermore, bulged iso-contours are observed in both the lower and upper corners of the open duct due to the presence of secondary flows in these regions. To elaborate on this, the magnitude of the mean cross-stream flow velocity ($\sqrt{V^{*2} + W^{*2}}$) and the corresponding vectors are given in the right-hand panel of Fig. 2(b). In the region below the bisector of the right lower corner, a lower secondary flow is observed with its rotation center located at position “D” shown in Fig. 2(b). This phenomenon resembles that observed in closed duct flows [42, 44]. In the right upper corner region, a small clockwise-rotating inner secondary vortex appears with its rotation center at position “A” in Fig. 2(b). This inner vortex can circulate fluid momentum between the side wall and the free surface, resulting in the deformed isotachs and thickened side wall boundary layers. Outside the inner secondary flow and above the lower secondary flow, a large-scale outer secondary vortex is observed. It contains two rotation centers (points “B” and “C” in Fig. 2(b)) and is responsible for transporting low momentum fluid from the lower side wall towards the free surface. These observations align well with previous literature on open duct flows [28-30, 45]. In addition, it is found that the maximum of the cross-stream secondary flow velocity is located on the free surface, with its value reaching 4.3% of the mean streamwise velocity. This finding is consistent with Nikitin’s research [29] on turbulent open rectangular duct flows.

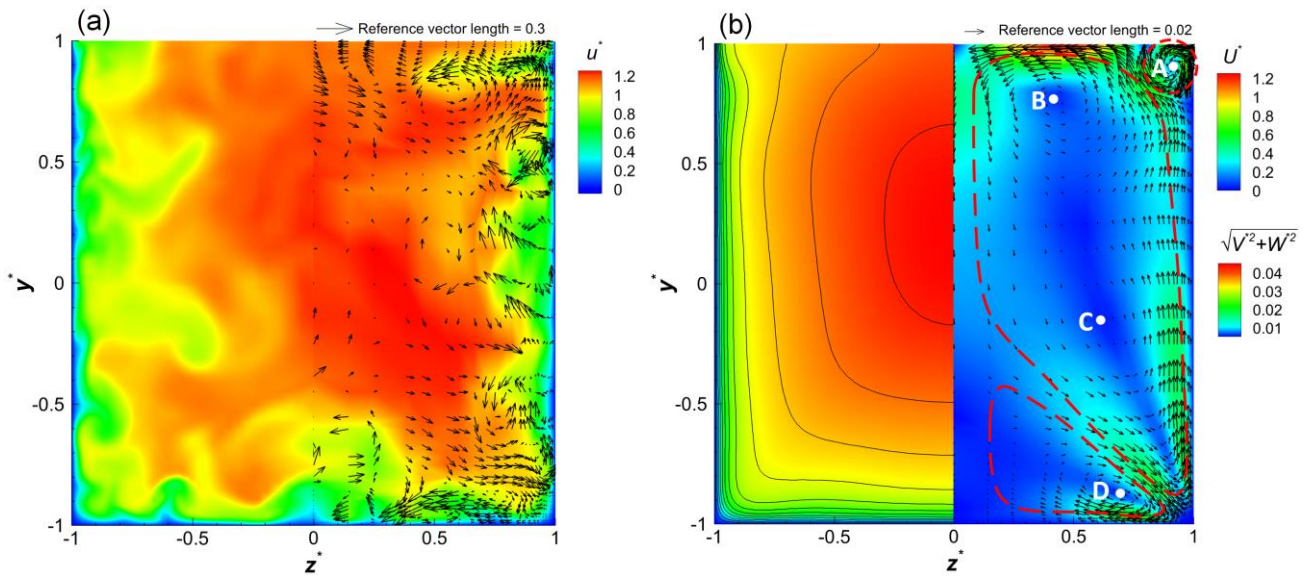
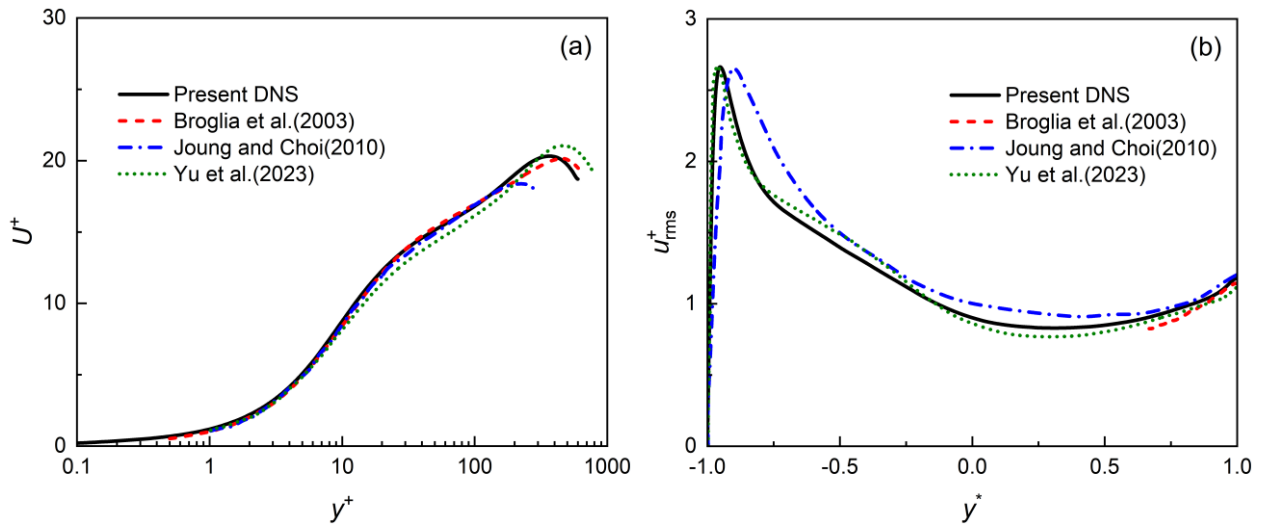


Fig. 2. Contours of the (a) instantaneous and (b) mean streamwise and cross-stream flow velocities overlaid with the

corresponding secondary flow vectors in the cross-sectional plane of the open duct.

Profiles of mean flow statistics normalized by the mean friction velocity along the bottom wall centerline are presented in Fig. 3. The results are compared with previous DNS results of Joung and Choi ($Re_\tau = 150$) [45], Yu et al. ($Re_\tau = 397$) [30], and the LES results near the free surface from Broglia et al. ($Re_\tau = 300$) [28]. In contrast to canonical wall-bounded turbulent flows, the mean streamwise velocities in Fig. 3(a) exhibit a peak before decreasing to a slightly lower value in open duct flows, indicating the presence of the velocity-dip phenomenon. Moreover, the maximum mean streamwise velocity increases with increasing Reynolds number. The present DNS results for the mean streamwise velocity agree well with the LES results of Broglia et al. [28] at the same Reynolds number, except for a small discrepancy near the free surface. This discrepancy can be attributed to the LES approach used by Broglia et al. [28], which underestimates secondary flow strength due to the sub-grid model and lower grid resolution employed in their study. Consequently, the position of maximum streamwise velocity obtained by Broglia et al. [28] is closer to the free surface. The *r.m.s.* velocities are shown in Fig. 3(b-d). In higher Reynolds number flows, the peaks of all components are closer to the bottom wall in the lower half of the duct. As the free surface is approached, the streamwise and spanwise *r. m. s.* velocities increase, while the transverse component is significantly reduced, analogous to that in typical open channel flows [46]. Furthermore, it is noteworthy that the spanwise *r. m. s.* velocity exceeds the streamwise component at the free surface in open square duct flows. This is likely due to the strong spanwise secondary flow near the free surface, which effectively transfers more turbulence kinetic energy between the surface-normal and spanwise directions. In conclusion, despite local small differences and Reynolds number effects, the present DNS results align well with previous literature data and provide confidence in the validity of the numerical approach employed.



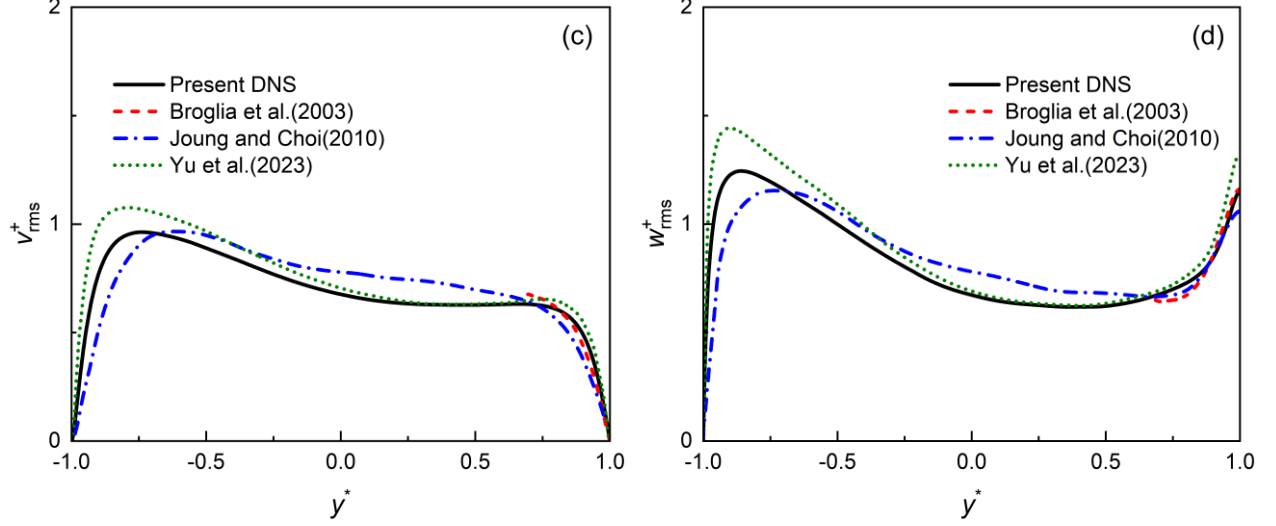


Fig. 3. Profiles of (a) the mean streamwise velocity and (b) streamwise, (c) transverse, and (d) spanwise components of *r. m. s.* velocities along the bottom wall centerline compared with previous literature data [28, 30, 45].

3. Results and discussion

Particles were injected into the flow field once fully developed turbulence was achieved. The concentration of particles in the viscous sublayer of all duct walls was continuously monitored until it reached a statistically stationary state, which was found to be achieved at $t^* = 1000$ in the present study. Subsequently, an additional 500 convection time units of data were collected to calculate the mean statistics of the particulate phase. To obtain the Eulerian statistics of the particulate phase, a non-uniform two-dimensional grid [18] was applied to the cross-section of the open duct. The mean statistics of the particulate phase can then be determined by using the same spatial and temporal averaging method employed for the fluid phase.

3.1. Instantaneous particle distribution and particle trajectories

The instantaneous particle distributions for different particle Stokes number at the end of the simulations are displayed in Fig. 4. As anticipated, the lightest $St^+ = 0.31$ particles distribute uniformly both in the duct cross-section and in the near-wall regions due to their low inertia. In contrast, the heavier $St^+ = 25$ particles tend to be predominantly segregated and form coherent clusters (highlighted with red circles in Fig. 4 (b)) near the walls, which correspond to the elongated streamwise particle streaks (marked with red lines) in Fig.4 (f) and (j). These particle streaks have previously been shown to concentrate preferentially in the low-speed-streamwise regions of the fluid flow [33], which are caused by the coherent turbulent vortices within these areas, as observed in Fig. 2(a). With further increases in Stokes number, particle motions become more inertial to these turbulent vortices, and the number

of particle streaks gradually reduces as evidenced in Fig. 4(g-h) and (k-l). It is also apparent that $St^+ \geq 25$ particles accumulate strongly in the bottom corners and form long particle streaks throughout the length of the duct, which is a consequence of the combined effects of the lower secondary flow and the outer secondary vortex shown in Fig. 2(b). In contrast, the upper corners of the mixed boundaries are relatively devoid of these heavier particles. This can be explained by the fact that the strong inner secondary vortex can entrain most of the heavier particles from the free surface to the lower part of the side walls. In comparison with the near-wall regions, it is visually apparent that there is a significantly lower concentration of heavier particles near the free surface. Nevertheless, these particles still distribute non-uniformly in the vicinity to the free surface and they were found to preferentially accumulate in regions where the instantaneous transverse secondary velocities are negative. More detailed information about the underlying mechanisms of particle accumulation near the free surface in turbulent open square duct flows can be found in the study by Wang et al. [33].

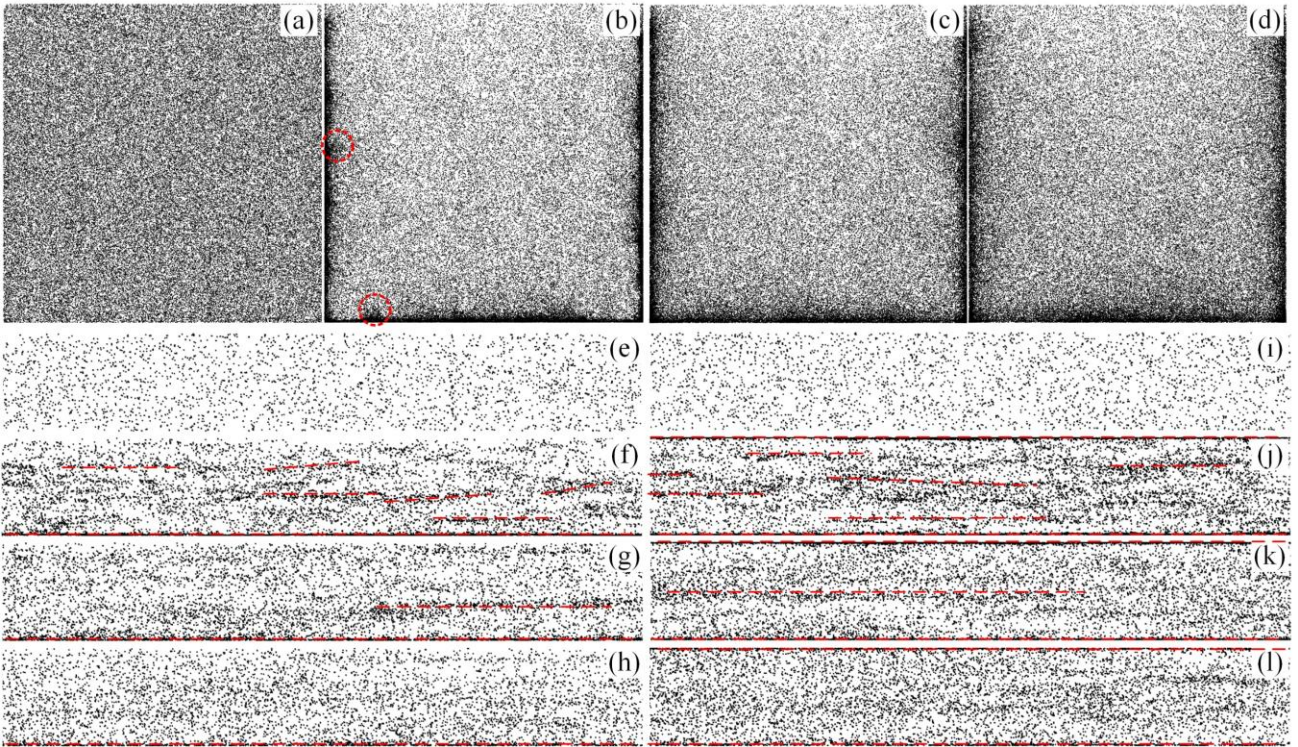
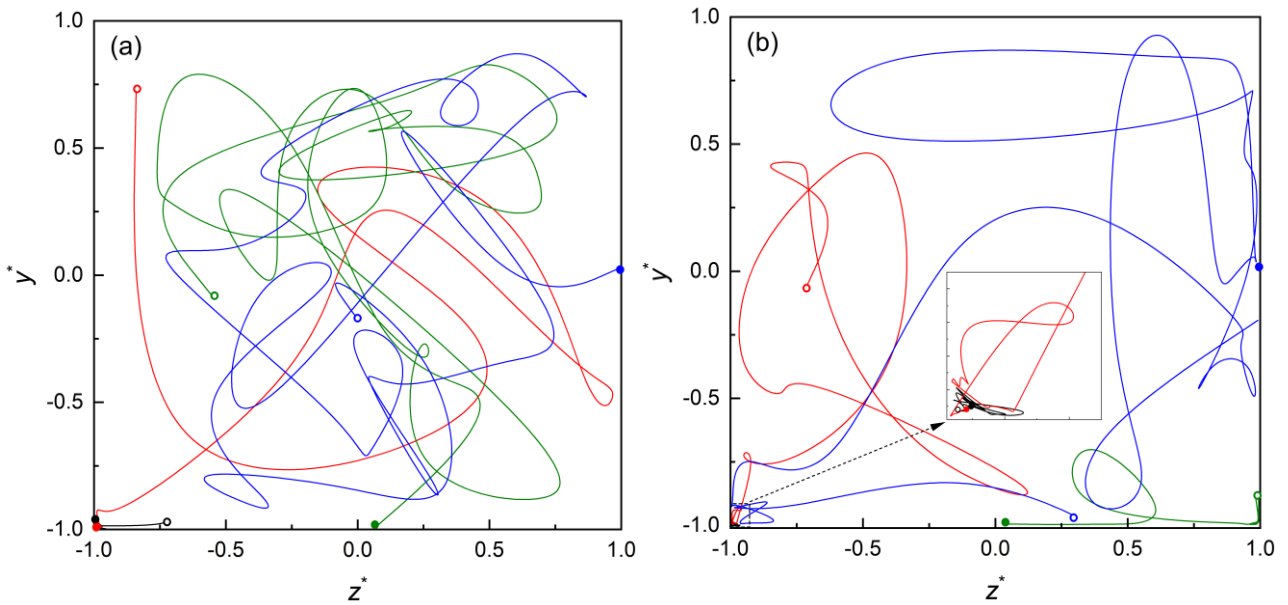


Fig. 4. Instantaneous particle distributions (a-d) projected in the cross-sectional plane of the open duct, near (e-h) the side walls ($z^+ \leq 30$) and (i-l) the bottom wall ($y^+ \leq 30$) for particles with (a, e, i) $St^+ = 0.31$, (b, f, j) $St^+ = 25$, (c, g, k) $St^+ = 125$, and (d, h, l) $St^+ = 260$.

Some typical trajectories of the indicated particles within the last 1000 convection time units of the simulations are shown in Fig. 5. It is evident that the lightest particles with $St^+ = 0.31$ are highly responsive to the instantaneous

cross-sectional vortices, resulting in an extended travel time towards the walls. In contrast, heavier particles with $St^+ \geq 25$ are more prone to being trapped near the walls. Even when trapped in the viscous sublayer, these particles exhibit slow back and forth motion along the wall in an oscillatory manner, which is linked to the modulation of the wall-parallel secondary flows. Furthermore, as shown in Fig. 5(b) (see the local enlarged area), the trajectory of $St^+ = 25$ particles in the buffer layer region of the lower duct corners indicates that they closely follow the instantaneous secondary flow structures and tend to cluster along these flow trajectories. Particles distributed near the outer edge of these secondary flow structures are easily entrained by the first coherent ejection events from the corner and then leave this region. However, the trajectory of $St^+ = 125$ particles in the same area suggests that they seem to be decoupled from the instantaneous flow structures and ultimately enter the stagnation region of the secondary flow, where the secondary velocity almost disappears. Therefore, these particles have no opportunity to escape from this area again and remain trapped here for a long time. The particle behavior observed in the lower duct corners is similar to that seen in closed duct flows [17, 18]. From an overall perspective of the entire duct cross-section, the inertial particles roughly follow the mean secondary flow cells performing a spiral motion throughout the duct, and they can be captured by different secondary cells during this process. In addition, note that the heavier particles rarely approach and reside near the free surface, which is likely related to the strong hindering force caused by the secondary flow there.



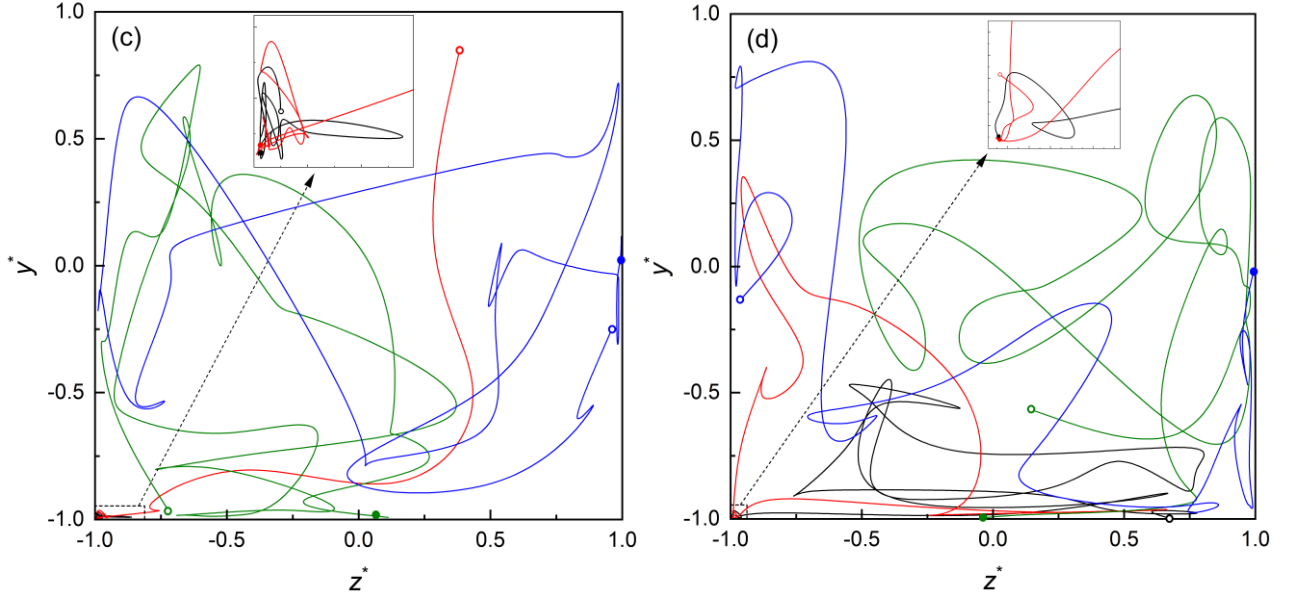


Fig. 5. Some typical particle trajectories projected in the cross-sectional plane of the open duct: (a) $St^+ = 0.31$, (b) $St^+ = 25$, (c) $St^+ = 125$, and (d) $St^+ = 260$. The open circle indicates the beginning of the track and solid circle denotes the final time of the trajectory. Different colors represent various particle tracks. All trajectories span a time interval of 1000 integral units.

3.2. Particle concentration and velocities

The cross-stream secondary flows shown in Fig. 2 are a result of the time and space averaging procedure. To fully understand their impact on particle dynamics, it is essential to analyze the average Eulerian statistics of the particulate phase. Fig. 6 shows contours of time-and space-averaged particle concentration normalized by the mean particle concentration using a logarithmic scale for different Stokes numbers. Similar to closed duct flows [18], the maximum concentration for heavier particles is found in the lower duct corners, with weakened accumulation levels as the Stokes number increases. Combined with Fig. 2(b), it is observed that the mean concentration of heavier $St^+ \geq 25$ particles is higher in regions where the mean streamwise flow velocity gradient is larger, a phenomenon significantly influenced by the mean secondary flow. Accordingly, the relatively low particle concentration near the free surface can be attributed not only to differences in turbulent structures compared to those in the near-wall regions [47], but also to the convection effect of the mean secondary flow there. Additionally, note that in the upper corner regions, the concentration contours of heavier particles exhibit a similar topological structure to that of the flow streamwise velocity contour, which also indirectly demonstrates the influence of the mean inner secondary vortex in this area. These observations further confirm those made in relation to the results presented in Fig. 4. Based on the analysis presented in Figs. 4-6, it can be concluded that heavier particles with $St^+ \geq 25$ tend to accumulate in the

lower corners of the duct as well as in the low-speed-streamwise regions of the fluid located in the middle areas of both sidewalls and the bottom wall. In contrast, these particles are absent from the upper corners and regions near the free surface. Therefore, a detailed analysis of mean particle dynamics in these specified regions will be conducted next.

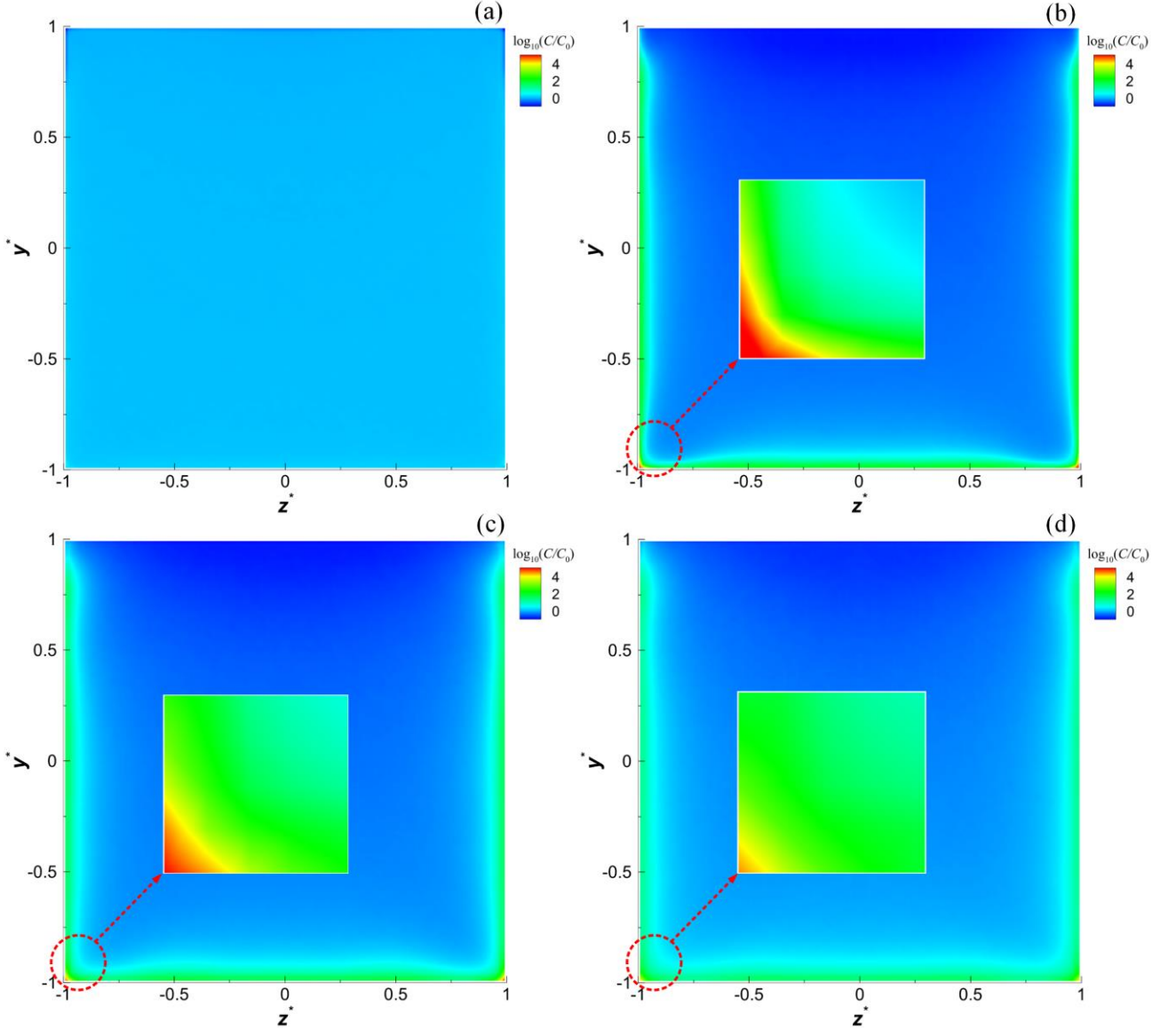


Fig. 6. Logarithmic representation of the contours of the average normalized particle concentration in the duct cross-section for various particle Stokes numbers: (a) $St^+ = 0.31$, (b) $St^+ = 25$, (c) $St^+ = 125$, and (d) $St^+ = 260$.

Fig. 7 shows contours of the mean streamwise particle velocity and the cross-stream particle velocity in the duct cross-section, with the latter overlaid with the corresponding vector fields in the left half panel. Additionally, Fig. 8 provides contours of the mean relative slip velocity ($\vec{u}_s^* = \vec{u}^* - \vec{u}_p^*$, $u_{s,yz}^* = \sqrt{u_{s,y}^{*2} + u_{s,z}^{*2}}$) between the two phases

corresponding to Fig. 7, which highlights the disparity between the particle dynamics and fluid tracers. Upon comparison with Fig. 2(b), it is evident that the cross-stream velocity distribution of the $St^+ = 0.31$ particles is analogous to that of the fluid phase. Nevertheless, it can still be discerned from Fig. 8(a) that the absolute value of the mean cross-stream slip velocity for the $St^+ = 0.31$ particles is relatively large near the walls and the free surface, reaching its maximum in the upper-corner regions near the free surface, with a magnitude on the order of 10^{-4} . Similar observations can be made for the heavier particles. This implies that inertial particles more easily decouple from the secondary flows in these regions. As the Stokes number increases, the absolute value of cross-stream slip velocity between the two phases also increases, as observed in Fig. 8(a-d). In fact, the ability of particles to follow the secondary flow is dependent on particle inertia and the position of the secondary flow vortex in the duct cross-section. Specifically, in the lower half of the duct, for particles with $St^+ = 25$ as shown in Fig. 8(b), the direction of the cross-stream slip velocity vectors points to the central area of the duct cross-section, implying that these velocities are higher than that of the fluid phase along the bisector of the bottom corner in the region of $y^*(z^*) < -0.5$. However, for particles with $St^+ \geq 125$, their cross-stream velocities are lower than those of the fluid phase in the same area, which explains why there is a higher concentration of $St^+ = 25$ particles in the lower corner regions, as presented in Fig. 6. In the upper half of the duct, near the wall-side of the inner secondary vortex (highlighted with a rectangular box in Fig. 7(a)), the absolute value of the cross-stream particle velocity gradually decreases with increasing Stokes number. Furthermore, because heavier particles are more inertial to the inner secondary vortex, the direction of their transverse cross-stream velocities becomes opposite to that of the fluid phase in this region, as shown in Figs. 7(b-d). Along the free surface in the spanwise direction, the dependence of the particle cross-stream velocity on Stokes number is similar to that near the inner secondary vortex. In particular, near the intersection of the inner and outer secondary vortices (highlighted with a dashed ellipse in Fig. 7(b)), the transverse velocities for all particles are larger than those of the fluid phase (resulting in negative slip velocities along the transverse direction, as seen in Fig. 8). Their dependence on particle inertia resembles that mentioned earlier in relation to those along the bottom corner bisector, with the maximum transverse velocity observed for particles with $St^+ = 25$. This suggests that in regions where two secondary vortices intersect, and their directions both converge towards the boundaries, the secondary flows no longer control the inertial particle trajectories, with the particles subsequently clustering near the boundaries.

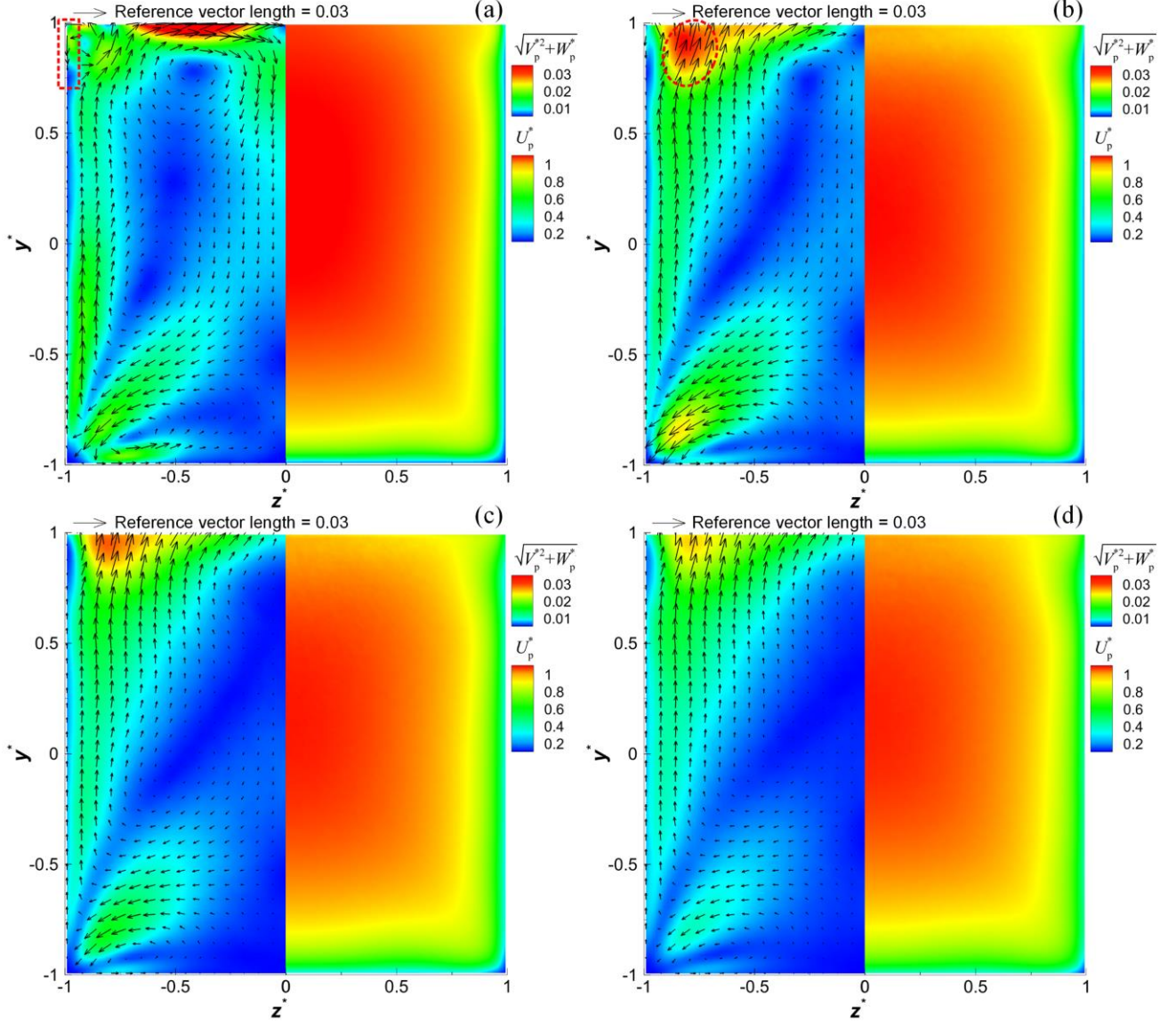


Fig. 7. Contours of the magnitude of the mean cross-stream particle velocity superimposed with its corresponding vector field in the left hand panel, with the mean streamwise particle velocity in the right hand panel for various particle Stokes numbers: (a) $St^+ = 0.31$, (b) $St^+ = 25$, (c) $St^+ = 125$, and (d) $St^+ = 260$.

In terms of the streamwise particle velocity, it is seen from the right half panel of Fig. 7 that their contours are analogues to that of the fluid phase, and their magnitude decreases with increasing Stokes number in the central region of the duct cross-section. As shown in the right half panel of Fig. 8(a), particles with $St^+ = 0.31$ in the viscous sublayer and part of the buffer layer move faster than the fluid phase. This phenomenon is primarily attributable to strong, near-wall coherent sweep events, which can propel particles with high streamwise momentum from the outer layer towards the near-wall region, although most of their streamwise momentum is suppressed during this process [18]. A similar behavior is also observed for particles with $St^+ \geq 25$. Furthermore, for these heavier particles in the

lower corner regions (refer to the area within the enclosed red dash line in Fig. 8(b)), the secondary flow also significantly contributes to their larger streamwise velocity compared to that of the fluid phase. This can be explained by the fact that the corner-directed secondary flow can carry high-momentum particles from the duct core region towards the corners, and upon entering the near-wall region, these heavier particles retain their high momentum obtained from the flow due to their high inertia. A similar phenomenon is also observed in the upper-corner regions. However, the influence of the secondary flows on particle motion gradually weakens as the Stokes number further increases. Moreover, it is observed that for the various Stokes numbers considered, there is an initial decrease followed by an increase in the range of near-wall regions where the particle streamwise velocity exceeds that of the fluid phase, as depicted in Fig.8 (a-d). The minimum range is observed for particles with $St^+ = 25$. This can be attributed to the preferential accumulation of heavier particles in low-speed-streamwise regions within the buffer layer of wall-bounded turbulence, with the highest accumulation level found for particles with $St^+ = 25$. In the middle area near the free surface, the streamwise velocity for heavier particles is smaller than that of the fluid phase due to their higher inertia.

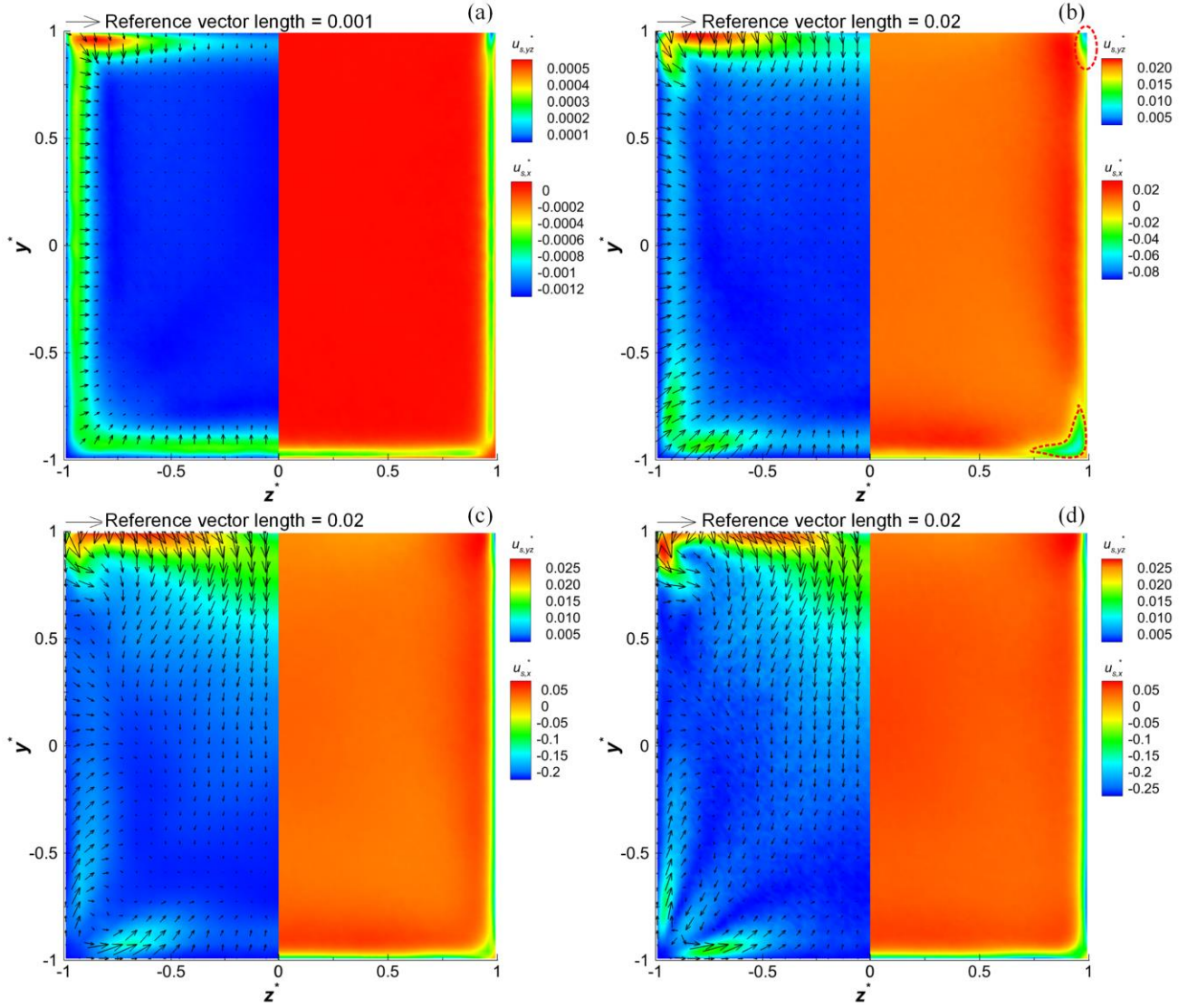


Fig. 8. Contours of the magnitude of the mean relative cross-stream slip velocity superimposed with its corresponding vector field in the left hand panel, with contours of the mean streamwise slip velocity in the right hand panel for various particle Stokes numbers: (a) $St^+ = 0.31$, (b) $St^+ = 25$, (c) $St^+ = 125$, and (d) $St^+ = 260$.

3.3. Particle acceleration

It has been previously demonstrated that particle acceleration statistics can be significantly affected by cross-stream secondary flows [17, 48]. Therefore, the mean statistics of particle acceleration are also discussed in this subsection. In correspondence to Fig. 8, the distribution of the mean cross-stream and streamwise particle acceleration are shown in the left and right half panels of Fig. 9, respectively. To provide a quantitative comparison of the streamwise and transverse components of particle acceleration between different particle populations, the profiles along the bottom wall centerline extracted from Fig. 9 are plotted in Fig. 10. Note that the overall distributions of the

mean streamwise particle acceleration qualitatively resemble those of the mean slip velocity shown in Fig. 8. It can be further observed from Fig. 10(a) that the streamwise acceleration is uniform over a large portion of the duct cross-section ($-0.7 < y^* < 0.7$) and exhibits similar values for the various particle sets, with the exception of the areas near the upper and lower boundaries. Near the bottom wall, the profile of the streamwise acceleration for $St^+ = 0.31$ particles shows a negative peak in the buffer layer at about $y^*(y^+) = -0.975(7.5)$. In contrast, the heavier particle sets ($St^+ \geq 25$) do not exhibit a minimum in the buffer layer but show a positive maximum at approximately $y^*(y^+) = -0.842(47.4)$. This behavior differs significantly from particle acceleration statistics in canonical channel flows [49], which can be ascribed to the non-alignment of the flow shear and wall-normal secondary flow along the bottom wall centerline [17,48]. Compared to the near-wall region, the magnitude of the streamwise particle acceleration in proximity to the free surface is significantly smaller. Furthermore, its value decreases with increasing particle inertia, although it remains positive. These findings reveal a distinctive particle acceleration behavior near the free surface.

With respect to the mean cross-stream particle acceleration, the distributions are again analogous to those of the mean slip velocity across the duct cross-section, except for in the near-wall region. This similarity suggests that the contributions to acceleration from the cross-sectional drag force are dominant in these regions for all particle sets, which will be discussed in detail later in Section 3.4. In the near-wall viscous sublayer (see the regions marked with a rectangular box in Fig. 9(c)), the direction of the cross-stream acceleration for heavier particles ($St^+ \geq 25$) points towards the wall, which primarily results from the significant contribution to acceleration from the shear-induced lift force. Additionally, it is observed from Fig. 10(b) that the transverse component of particle acceleration has a positive peak near the bottom wall and a negative peak near the free surface. The magnitude of these extreme values decreases with increasing Stokes number, which is in accordance with observations in closed square duct flows [17]. Moreover, note that the absolute value of the positive peak near the wall is significantly larger than that of the negative peak near the free surface for the $St^+ = 0.31$ particles. However, for heavier particles with $St^+ \geq 25$ the opposite trend is observed (refer to the local enlarged view of Fig. 10(b)). It is also worth noting that the transverse accelerations for all particle sets are negative along the bottom wall bisector in the region of $y^* \geq -0.75$. These findings imply that in the present open duct flow, the cross-stream secondary motions contribute to accelerating the low-inertia particles away from the bottom wall in the region $y^* < -0.75$, while simultaneously decelerating high-inertia particles approaching the free surface within the region $y^* > 0.75$ in the transverse symmetry plane. Owing to the symmetry, the mean spanwise acceleration values in the transverse symmetry plane are zero.

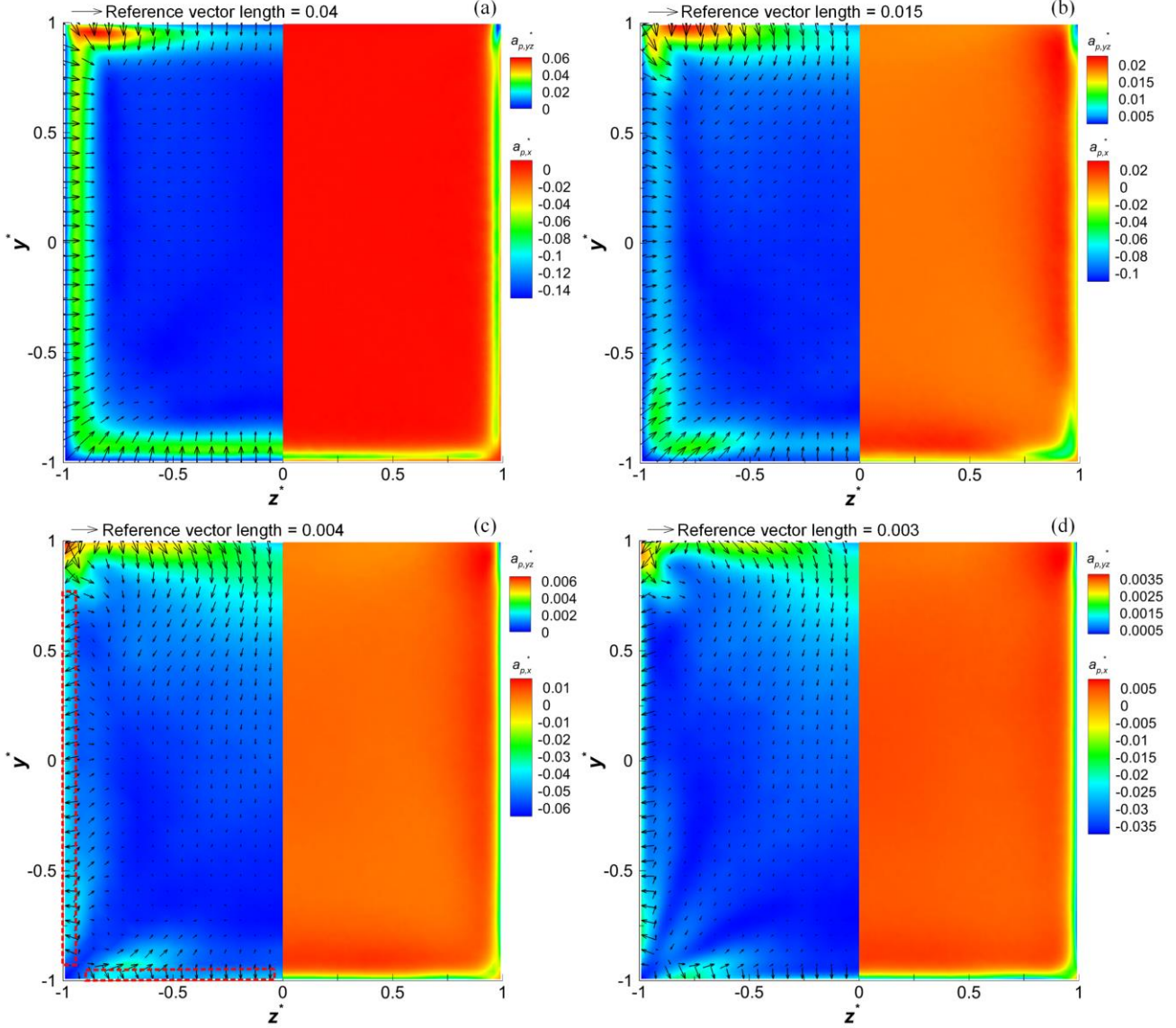


Fig. 9. Contours of the magnitude of the mean cross-stream particle acceleration superimposed with its corresponding vector field in the left half panel, with contours of the mean streamwise particle acceleration in the right hand panel for various particle Stokes numbers: (a) $St^+ = 0.31$, (b) $St^+ = 25$, (c) $St^+ = 125$, and (d) $St^+ = 260$.

It should be noted that the secondary flow in the transverse symmetry plane has an opposite impact on particle acceleration behavior near the wall and the free surface. As aforementioned, the peak magnitude of particle acceleration both in the streamwise and transverse directions near the bottom wall can be significantly reduced due to the presence of the upward secondary flow in closed square duct flows [17]. In turbulent open wall-bounded flows, as the free stream where turbulence is nearly isotropic is approached, mean particle acceleration should be zero [50]. However, in contrast, an obvious peak in particle acceleration near the free surface appears in the current open duct flow, which is most likely due to the influence of the downward secondary flow normal to the surface. This indicates

that the secondary flow induced by turbulence anisotropy near the free surface can encourage particle acceleration, with this effect being less pronounced for heavier particles. Overall, in comparison with closed square duct flows, the presence of a weak shear free-slip boundary in the present open duct flow can somewhat reduce the peaks in particle acceleration near the bottom wall. Additionally, due to the inertia dependence of particle motion on the secondary flow [48], whose topology and intensity is different near the wall and the free surface, the absolute value of the transverse acceleration peak for $St^+ = 0.31$ particles is higher near the wall than near the free surface. Conversely, for the heavier particles, the corresponding value near the wall is lower than that near the free surface.

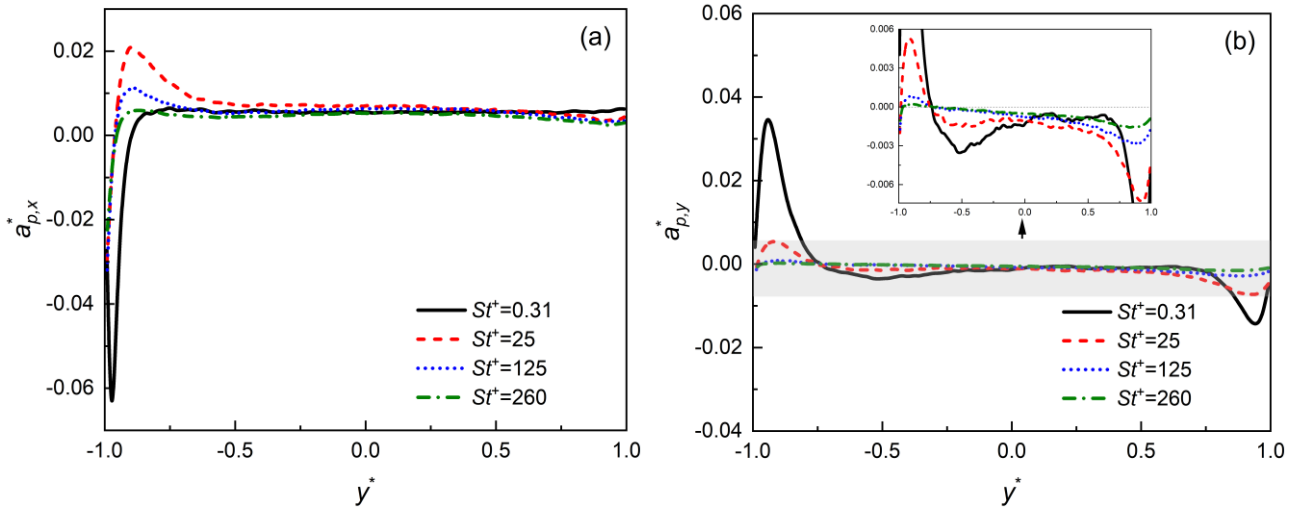


Fig. 10. Profiles of the (a) streamwise and (b) transverse components of the mean particle acceleration along the bottom-wall centerline.

Profiles of the streamwise ($a_{prms,x}^*$) and transverse ($a_{prms,y}^*$) components of the *r.m.s.* of particle acceleration in the symmetry plane of the open square duct are displayed in Fig. 11. As observed in conventional particle-laden wall-bounded turbulent flows [49, 50], the streamwise component, $a_{prms,x}^*$, attains a maximum in proximity to the wall, with its value initially increasing with an increase in Stokes number until $St^+ = 5$, and subsequently decreasing as the particle inertia is further increased. The dependence of the $a_{prms,x}^*$ maximum near the wall on Stokes number in the current open duct flow aligns with this trend, although the position of the corresponding maximum from the wall varies for different particle sets. In contrast, the peak values of $a_{prms,y}^*$ near the wall are relatively low and decrease with increasing Stokes number, with a similar trend observed in the spanwise component of the mean

particle acceleration. These observations are consistent with the findings of Zamansky et al. [49] and Gerashchenko et al. [50] in turbulent channel flows. As the free surface is approached, $a_{prms,x}^*$ values for all particles sets reach a local peak, with this trend less pronounced for heavier particles. The transverse component, $a_{prms,y}^*$, also exhibits a peak near the free surface. However, these peak values near the free surface are significantly lower than those observed near the wall. This is reasonable given that the turbulence level near the wall is generally higher than that near the free surface. In comparison with turbulent wall-bounded flows [50], the occurrence of peaks in the *r.m.s.* of particle acceleration near the free surface in the present open duct flow is most likely due to the convection effects of the secondary flow. This can entrain particles with a higher turbulence level from the bottom wall region to the free surface, with its effect on particle acceleration weakened with increasing Stokes number in the transverse symmetry plane.

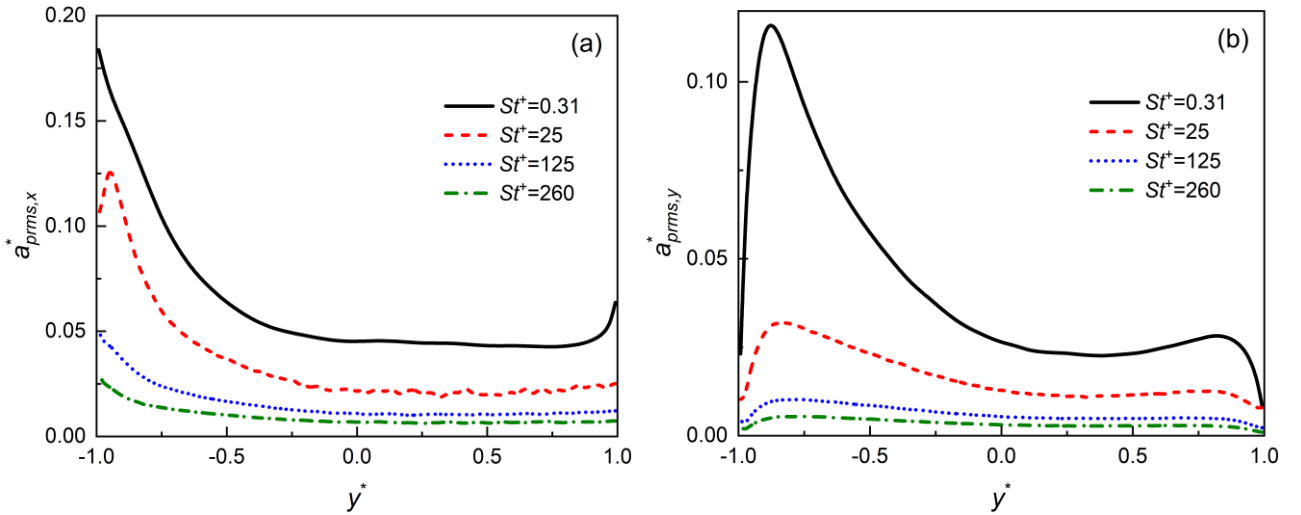


Fig. 11. Profiles of the (a) streamwise and (b) transverse components of the *r.m.s.* of the particle acceleration along the bottom-wall centerline.

3.4. Particle dynamics

To explore the particle dynamics in more detail, the contributions to particle motions from all considered forces are analyzed in this last subsection. The left hand panel of Fig. 12 illustrates contours of the magnitude of the dimensionless average cross-sectional drag force and the corresponding cross-sectional force vectors, with the distributions of the streamwise component of the mean drag force shown in the right hand panel. To quantify the effect of Stokes number, the profiles of the transverse and streamwise components of the drag force along the bottom

wall centerline are plotted in Fig. 13. In the lower half of the duct cross-section, the distribution of the cross-sectional drag force resembles that found in closed duct flows, where the magnitude of the cross-sectional drag force is relatively high and directed away from the wall in the near-wall region [18]. Similar observations can also be made near the side wall and free surface in the upper half of the duct cross-section. For heavier particles with $St^+ \geq 125$, the drag force is stronger in the upper-corner regions and the middle area of the free surface, which suggests that the secondary flow-induced cross-sectional drag force tends to discourage inertial particles from moving towards either the walls or the free surface. In Fig. 13(a), it is further noted that in moving upwards along the bottom wall centerline, the transverse component of the drag force first increases then decreases to zero at approximately $y^* = -0.75$. Subsequently, it reverses and becomes negative, with its magnitude gradually increasing to a maximum before decreasing again as the free surface is approached. As the Stokes number increases, the absolute value of the transverse drag force along the bottom wall centerline gradually increases, and its peak moves farther from the free surface. Such a distribution of the cross-sectional drag force is primarily influenced by the relative motion between the two phases, as discussed previously in relation to the results of Fig. 8.

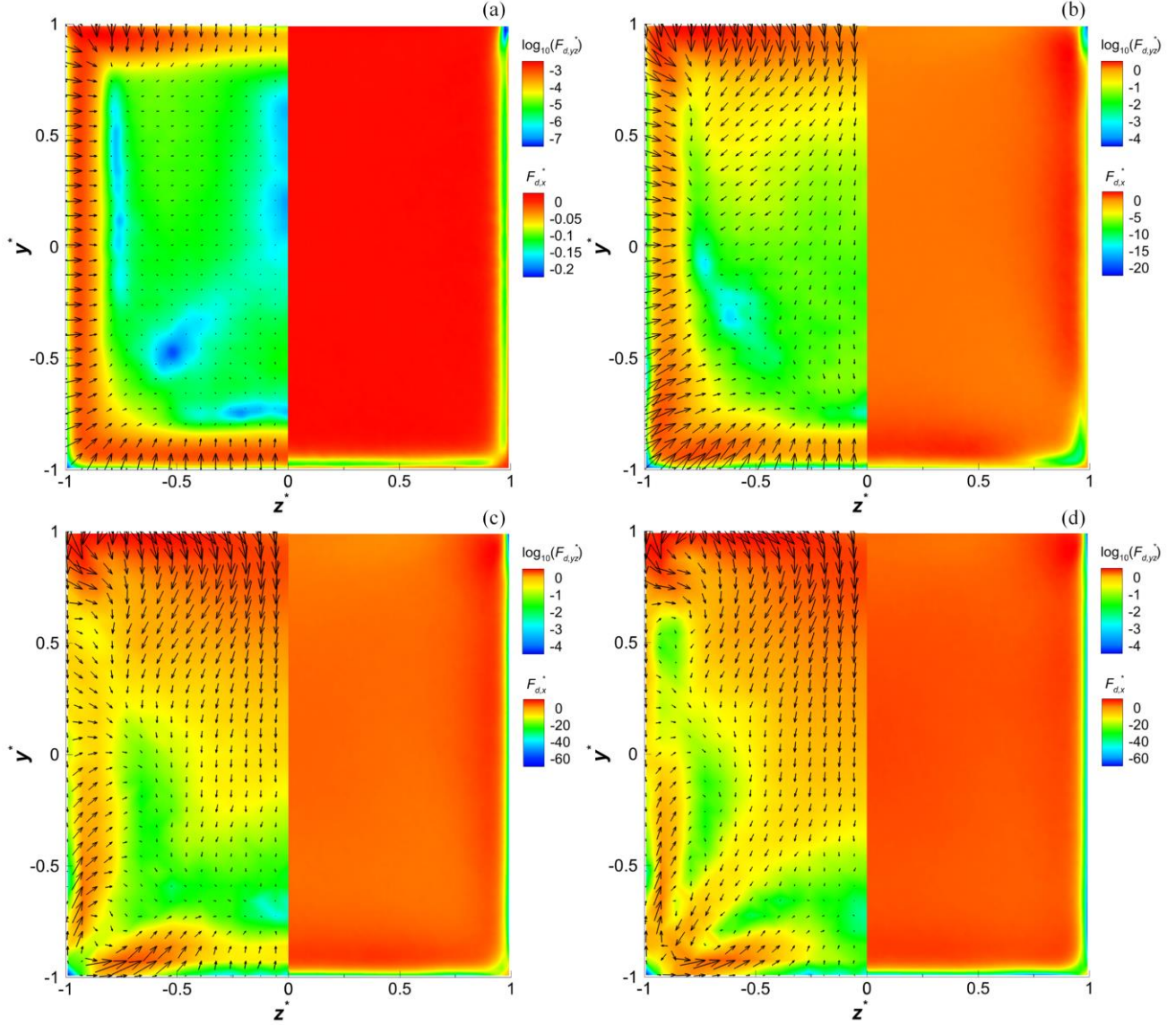


Fig. 12. Contours of the magnitude of the nondimensionalized average cross-sectional drag force (logarithmic values $\log_{10}(\sqrt{F_{dy}^{*2} + F_{dz}^{*2}})$) superimposed with its cross-sectional force vectors in the left hand panel, with the distribution of the mean streamwise drag force in the right hand panel for different particle Stokes numbers: (a) $St^+ = 0.31$, (b) $St^+ = 25$, (c) $St^+ = 125$, and (d) $St^+ = 260$.

In the streamwise direction, the drag force is evenly distributed in central regions of the duct cross-section. From Fig. 13(b), it is further observed that the streamwise drag force is positive in the region of $y^* > -0.95$ along the bottom wall centerline, indicating that the drag force acts as a driving force to push particles downstream. This is mainly due to particles lagging behind the fluid phase because of their inertia in these regions. Furthermore, it should be noted that there is a positive peak in the streamwise drag force both near the walls and the free surface. This can

be attributed to the large relative slip velocity caused by the particles' preferential sampling of slower-than-average fluid induced by the local turbulence and secondary flow in these regions. In contrast, in the near-wall region of $y^* < -0.95$, the particles move faster than the fluid phase due to the concurrent action of particle inertia and coherent events in near-wall turbulence, as explained in relation to Fig. 8. Therefore, the streamwise drag force is negative and acts to impede the forward motion of particles, with its magnitude increasing with particle Stokes number. These observations are in qualitative agreement with the work of Mortimer et al. [25] on channel flows.

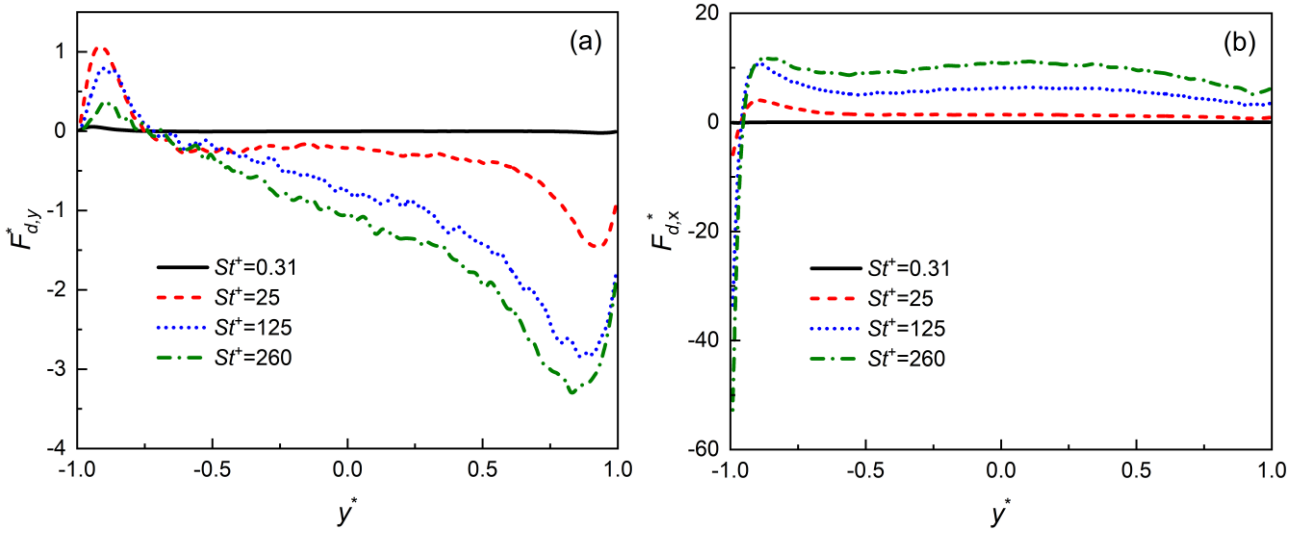


Fig. 13. Profiles of the (a) transverse and (b) streamwise components of the drag force along the bottom wall centerline.

The distribution of the average shear lift force in the duct cross-section and its profiles along the bottom wall centerline are displayed in Figs.14 and 15, respectively. It is evident from Fig. 14 that the cross-sectional shear lift force points almost perpendicularly to the walls, with its magnitude reaching a maximum at the wall due to the largest streamwise flow shear at this location. These findings are consistent with those reported by Wang et al. [18] and Winkler et al. [26] for closed duct flows. Near the side wall in the upper corner, the spanwise shear lift force is apparently greater than that in the lower corner. This can be attributed to the absence of an obvious stagnation area of secondary flow in the upper corner, in contrast to the lower corner. As a result, the strong convection of the inner secondary vortex facilitates the transfer of high-momentum fluid from the surface to the region very close to the upper corner, which ultimately results in a relatively large streamwise velocity gradient near the side wall in this region. Near the free surface, the cross-sectional lift force is also relevant but still relatively small compared to that

near the wall. As shown in the local enlarged view of Fig. 14(b), the direction of the cross-stream lift force points towards the surface, which reveals that it can promote inertial particles to move toward the free surface. The contributions to the shear lift force from the secondary flow velocity gradients also play a significant role in this region due to the low streamwise shear present here. In Fig. 14(a) it is further observed that along the bottom-wall centerline, the cross-sectional shear lift force for all particle populations reaches its negative minimum at the wall and a positive maximum at the free surface, with its magnitude increasing as the Stokes number increases. Within most areas of the duct cross-section ($-0.95 < y^* < 0.95$), the values of the cross-sectional shear lift force are, however, zero.

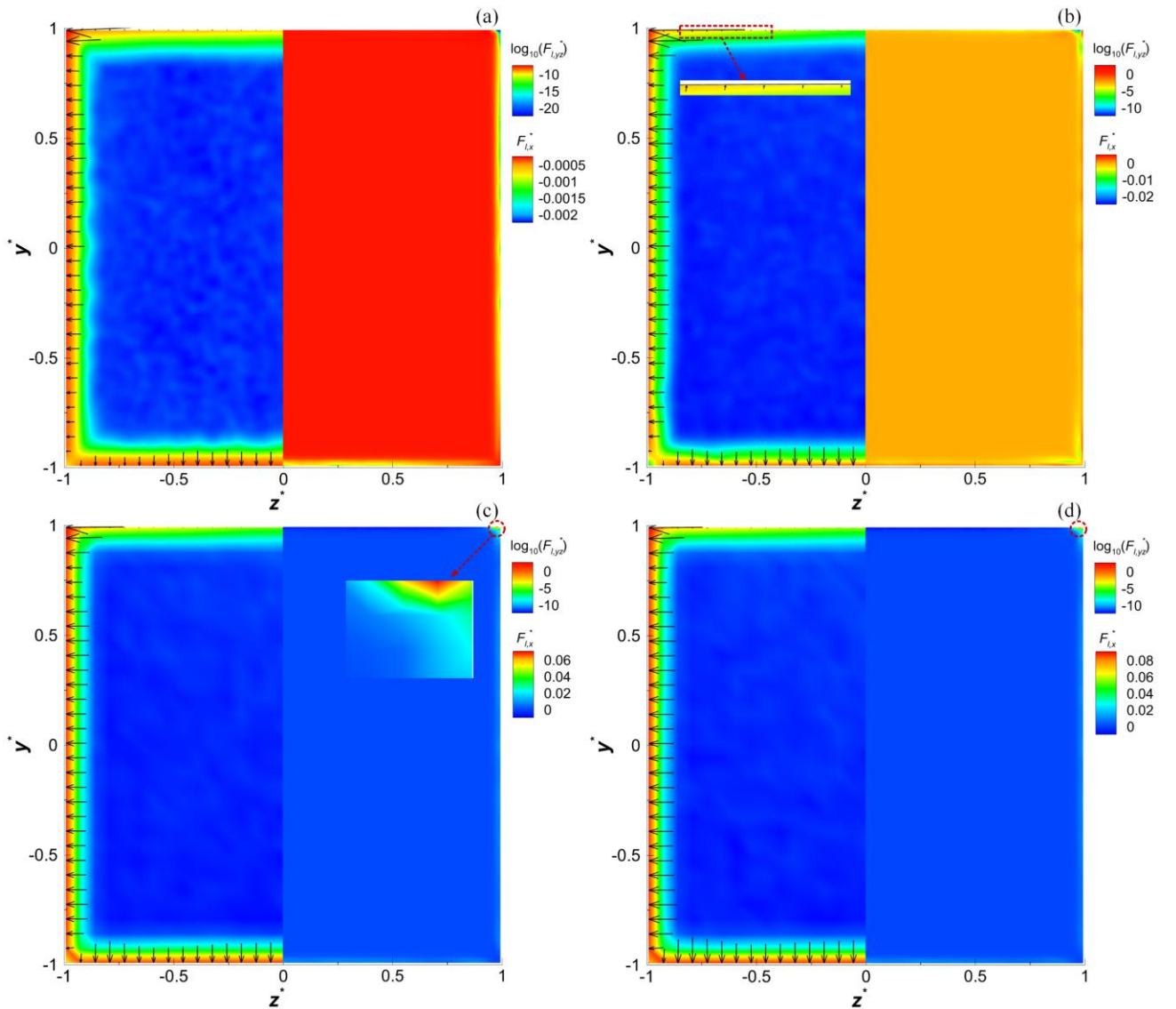


Fig. 14. Contours of the magnitude of the nondimensionalized average cross-sectional shear-lift force (logarithmic values $\log_{10}(\sqrt{F_{ly}^{*2} + F_{lz}^{*2}})$) superimposed with its cross-sectional force vectors in the left hand panel, with contours the mean streamwise lift force in the right hand panel for different particle Stokes numbers: (a) $St^+ = 0.31$, (b) $St^+ =$

25, (c) $St^+ = 125$, and (d) $St^+ = 260$.

The magnitude of the streamwise component of the shear lift force is significantly lower than that of the transverse component in the near-wall region, as demonstrated by the results shown in Fig. 14(b). This disparity can be attributed to the influence of the cross-sectional mean secondary slip velocity on the streamwise lift force, which has values significantly lower than the streamwise slip velocity for heavier particles in these regions. Near the free surface, the magnitude of the streamwise lift force is comparable to that of the transverse component. In particular, the local large streamwise lift force in the upper corner region, as seen in Fig. 14(c), is predominantly caused by the combined effect of high mean streamwise velocity gradients near the side wall and the mean cross-stream slip velocity. Furthermore, the streamwise lift force in the near wall region ($y^*(y^+) < -0.95(15)$) is positive, whereas in the surface region ($y^* > 0.95$) it becomes negative for heavier particles with $St^+ \geq 25$. These observations suggest that the cross-sectional lift force acts to propel particles towards the walls and the free surface, leading to an increase in particle concentration near these boundaries. Despite its small magnitude, the streamwise lift force near the walls tends to accelerate inertial particles, thereby mitigating particle accumulation in the streamwise direction to some extent. Conversely, the streamwise lift force near the free surface tends to decelerate particles and enhance particle preferential concentration in this region.

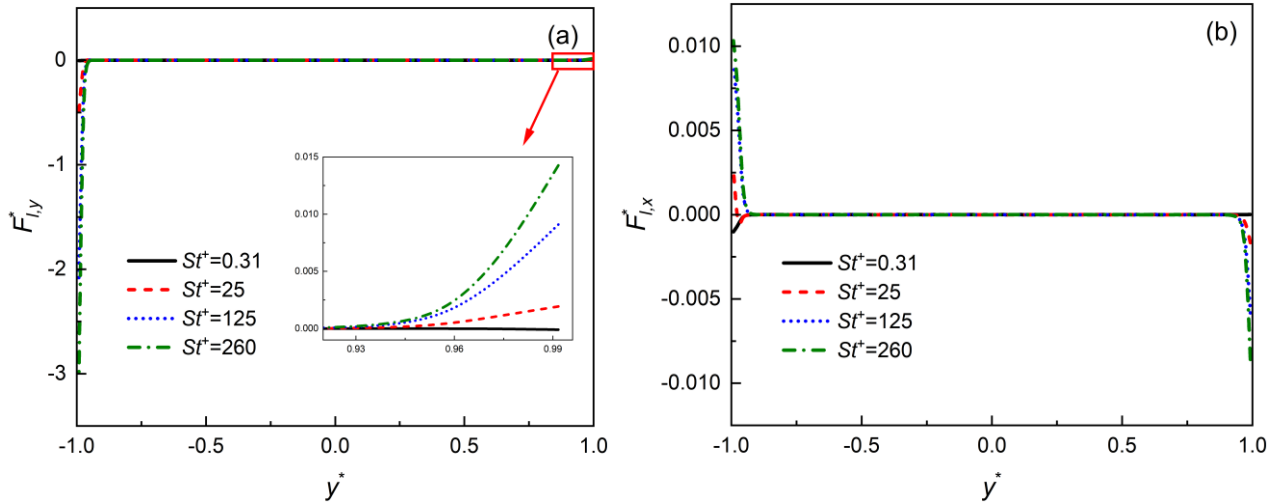


Fig. 15. Profiles of the (a) transverse and (b) streamwise components of the shear lift force along the bottom wall centerline.

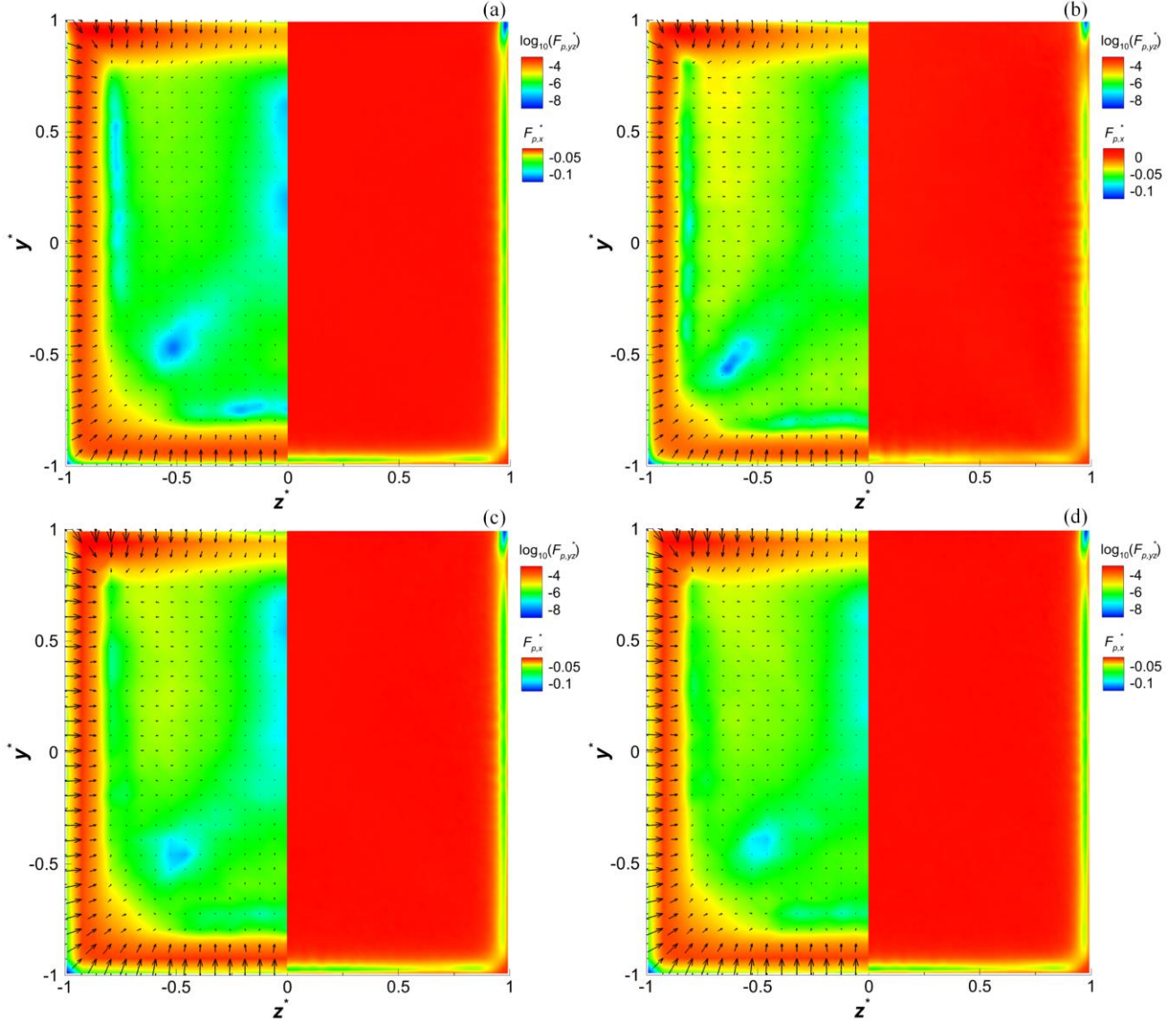


Fig. 16. Contours of the magnitude of the nondimensionalized average cross-sectional pressure gradient force (logarithmic values $\log_{10}(\sqrt{F_{py}^{*2} + F_{pz}^{*2}})$) superimposed with its cross-sectional force vectors in the left hand panel, with contours of the mean streamwise pressure gradient force in the right hand panel for different particle Stokes numbers: (a) $St^+ = 0.31$, (b) $St^+ = 25$, (c) $St^+ = 125$, and (d) $St^+ = 260$.

Figs. 16 and 17 present the distribution of the average cross-sectional pressure gradient force and its transverse and streamwise components along the bottom wall centerline, respectively, for each particle Stokes number. Since the pressure gradient force is mainly dependent on the local fluid acceleration, its distribution across the duct is similar for all particle sets. In regions near the walls or free surface where the secondary flow gradients are predominant, the cross-sectional pressure gradient force is strong and directed away from these boundaries. In the streamwise direction, the pressure gradient force is mainly significant in the near-wall viscous sublayer. Its largest absolute value is found in the upper-corner region, which is likely due to the large streamwise velocity gradients

induced by the inner secondary vortex there. Based on the results of Fig. 17, it is further confirmed that the difference in pressure gradient force between different particle sets is very small, except for particles with $St^+ = 25$ in the near-wall region. This is likely related to the strong preferential accumulation of $St^+ = 25$ particles in the buffer layer, which potentially leads to a lower fluid acceleration located at the particle positions. In general, the cross-sectional components of the pressure gradient force tend to encourage particle motions from the boundaries to the bulk flow region, whereas in the streamwise direction, the pressure gradient force acts to decelerate the particles in the near-wall region but accelerate them in the outer flow region. These findings agree well with the observations of Mortimer et al. [25] on channel flows and Wang et al. [18] on closed duct flows.

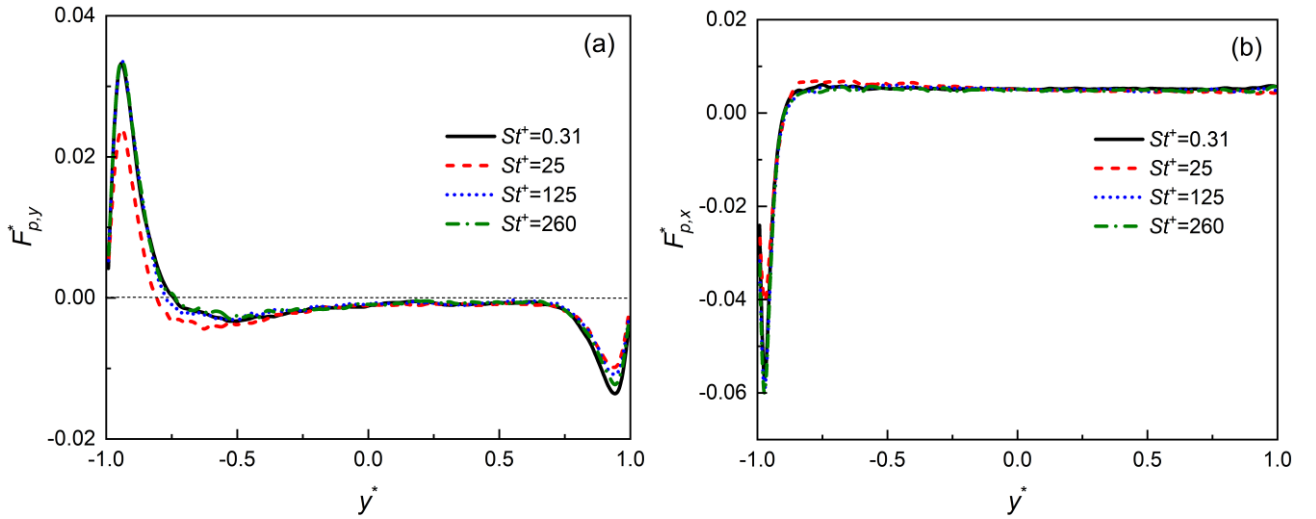


Fig. 17. Profiles of the (a) transverse and (b) streamwise components of the pressure gradient force along the bottom wall centerline.

Profiles of the transverse and streamwise components of the added mass force along the bottom wall centerline are illustrated in Fig. 18. The overall distribution of the added mass force in the duct cross-section is similar to that of the pressure gradient force for heavier particles with $St^+ \geq 25$, thus their contours are not shown here. For $St^+ = 0.31$ particles, their accelerations closely resemble those of the fluid phase due to their low inertia. As a consequence, the magnitude of the added mass force for these particles is small in comparison to that of the heavier particle sets. Notwithstanding this, it is apparent from Fig. 18(a) that the transverse component of the added mass force is negative in the near-wall region and positive near the free surface for $St^+ = 0.31$ particles, indicating that the cross-sectional added mass force tends to push particles towards the walls and free surface in the regions near these boundaries. Likewise, it can be inferred from Fig. 18(b) that the streamwise added mass force tends to accelerate particles with

$St^+ = 0.31$ in the near-wall region, a trend opposite to that of heavier particles in the same area. This is due to the fact that the magnitude of the acceleration peaks near the boundaries for $St^+ = 0.31$ particles is higher than that of the fluid both in the cross-stream and streamwise directions, which can be explained as follows. In the streamwise direction, inertial particles with $St^+ < 5$ may experience the intermittency of high-and-low speed streaks in the near-wall region where the fluid velocity variations are rapid, leading to a higher particle acceleration than the fluid phase [49]. Meanwhile, in the cross-stream directions, the presence of the secondary flow tends to cause low-inertia particles to have higher velocity fluctuations compared to the fluid phase along the bottom wall centerline [33], which may also contribute to the increased particle acceleration in these regions. As the Stokes number increases further ($St^+ > 5$), particles respond less to the fluid velocity variations and the discrepancy in acceleration between the two phases becomes more obvious, which consequently results in a greater added mass force for heavier particles.

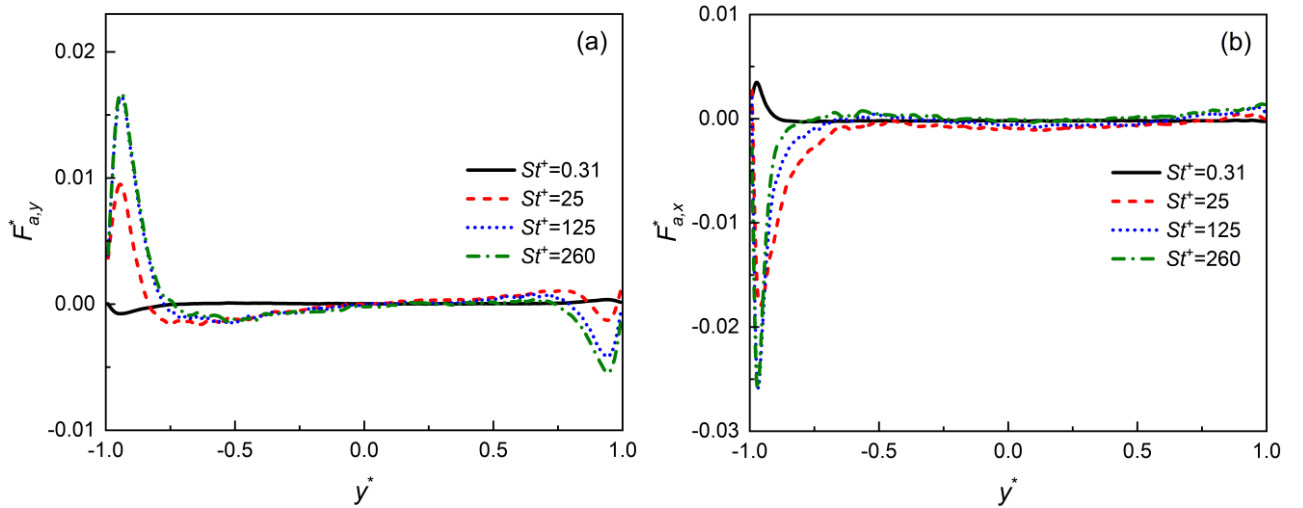


Fig. 18. Profiles of the (a) transverse and (b) streamwise components of the added mass force along the bottom wall centerline.

To quantify the relative importance of the various forces considered for each particle set, Fig.19 presents a comparison between the profiles of the transverse components of all considered forces acting on the different particle sets along the bottom wall centerline. It is obvious that the mean drag force induced by the secondary flow plays a dominant role across the duct cross-section for all given particle sets. For the low inertia $St^+ = 0.31$ particles, the pressure gradient force also makes an important contribution in regions near the walls and free surface. With an increase in Stokes number, the shear lift force becomes more significant in the near-wall viscous sublayer. Outside of this sublayer, for heavier particles with $St^+ \geq 25$, the influence of other forces can be neglected when compared

to the drag force. In the streamwise direction, the relative importance of these forces is basically similar to that in the cross-sectional plane, aside from the different dependence of shear-lift force on Stokes number in the viscous sublayer. In summary, the combined hydrodynamic forces act to repel particles from the boundaries towards the central regions of the duct cross-section in the cross-stream direction, and propel them forward in the streamwise direction. In the viscous sublayer, these forces work to confine particles to the near-wall region and decelerate their movement in the streamwise direction, ultimately leading to particle accumulation in these areas. The interaction of these hydrodynamic forces eventually results in a distribution of particle accelerations as displayed in Fig. 9.

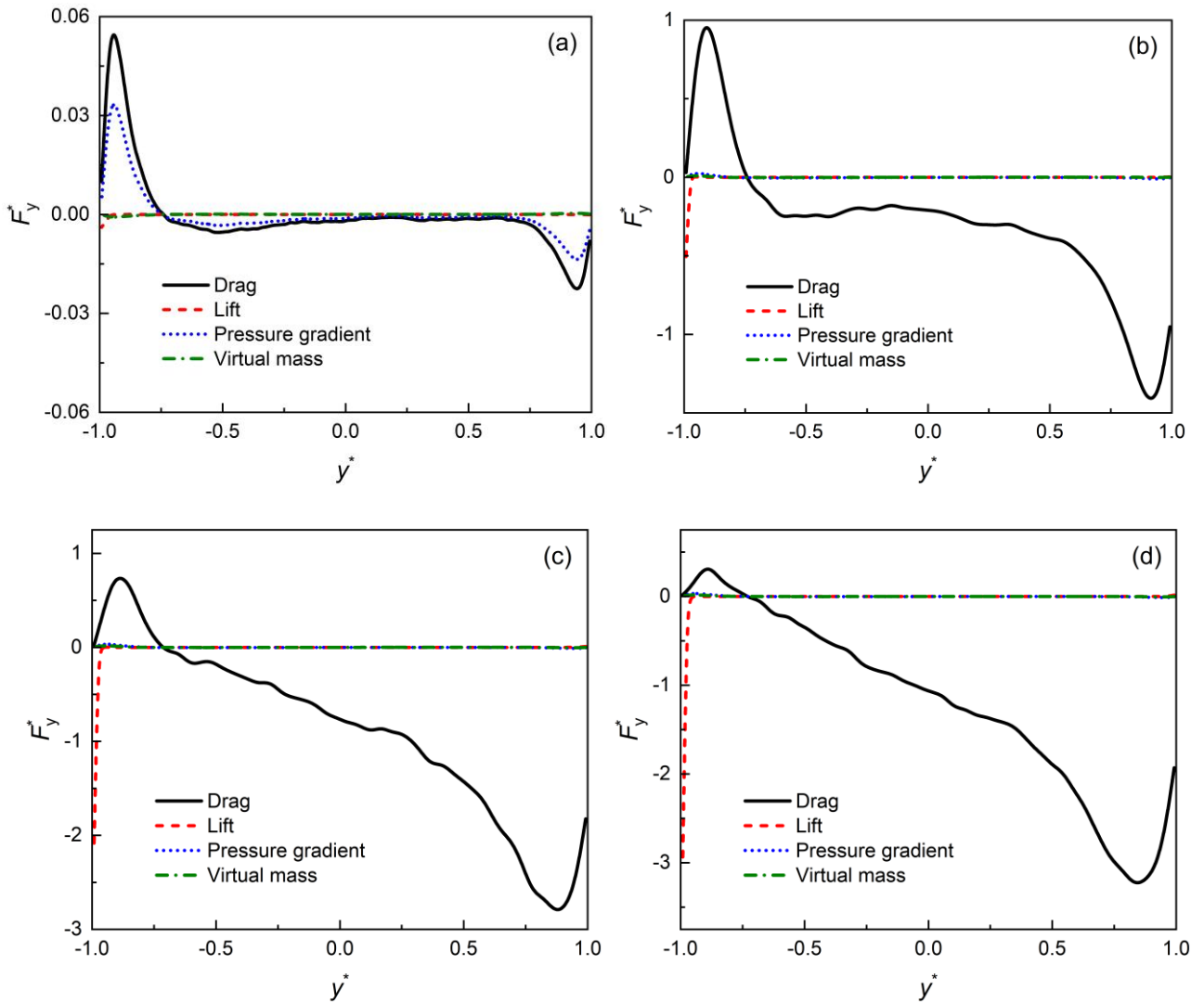


Fig. 19. Comparison between profiles of the average transverse component of all considered forces acting on the particles along the bottom wall centerline for particles with different Stokes numbers:(a) $St^+ = 0.31$, (b) $St^+ = 25$, (c) $St^+ = 125$, and (d) $St^+ = 260$.

4. Conclusions

Particle dynamics in a fully developed turbulent open square duct flow has been studied by means of direct numerical simulation combined with a one-way coupled Lagrangian particle tracking technique. The shear Reynolds number was 300, with corresponding particle Stokes numbers ranging from 0.31 to 260. The focus has concentrated on the secondary flow effects on particle dynamics across the duct cross-section, particularly near the walls and the free surface. The main conclusions are as follows:

- For the particle spatial distribution, low-inertia particles with $St^+ = 0.31$ distribute uniformly in the duct cross-section while heavier particles with $St^+ = 25$ tend to form elongated streamwise particle streaks in the near-wall regions, with this tendency less pronounced as the Stokes number increases further. In addition, heavier particles also accumulate intensely in the lower corners of the duct and form long particle streaks throughout its length. In contrast, there is a significantly lower concentration of heavier particles near the free surface, and the upper corners of mixed boundaries are relatively devoid of these particles.
- The ability of particles to follow the secondary flow is dependent on both particle inertia and the position of the secondary flow vortex in the duct cross-section. Along the bisector of the bottom corner in the region of $y^*(z^*) < -0.5$, particles with $St^+ = 25$ have higher cross-stream velocities than that of the fluid, while those with $St^+ \geq 125$ show lower cross-stream velocities than the fluid. Near the intersection of the inner and outer secondary vortices in the upper corners of the duct, the transverse cross-stream velocities for all particles exceed those for the fluid phase. In the streamwise direction, particles move faster than the fluid in the viscous sublayer and part of the buffer layer adjacent to the walls. However, in the middle regions of the flow near the free surface, heavier particles have a lower streamwise velocity than the fluid phase.
- For the cross-sectional particle accelerations, it is observed that along the bottom wall centerline, the transverse particle acceleration exhibits a positive peak near the bottom wall and a negative peak near the free surface, with the magnitude of these extreme values decreasing with increasing Stokes number. The secondary flow near the free surface is found to encourage particle acceleration, although this effect is less pronounced for the heavier particles. In the streamwise direction, the distribution of particle acceleration in the duct cross-section is relatively uniform and exhibits similar values for all particle sets. Compared to the near-wall region, the magnitude of the streamwise particle acceleration in proximity to the free surface is significantly smaller.
- In terms of particle hydrodynamics, the cross-sectional drag force near the walls and the free surface acts to discourage inertial particles from moving towards either the walls or free surface. Contrary to the effects of the

cross-sectional drag force, the cross-sectional shear lift force in the viscous sublayer, or very close to the free surface, encourages inertial particles to move toward the walls or free surface. In regions near the walls or free surface, the cross-sectional pressure gradient force tends to encourage particle motions from the boundaries to the bulk flow region, a similar behavior is observed for added mass force acting on heavier particles. Overall, the drag force is the dominant factor acting across the duct cross-section for all particle sets. As the Stokes number increases, the cross-sectional shear lift force becomes more dominant in the near-wall viscous sublayer. Beyond this sublayer, the influence of other forces is negligible compared to the drag force for heavier particles.

Since the particle concentration considered in the present open duct flow was relatively small, particle-induced effects on the flow turbulence have been neglected. However, when the particle volume fraction is relatively high, these effects cannot be ignored. Previous studies [51, 52] have identified a critical value for the particle volume fraction in turbulent closed duct flows at which such effects become significant. Below this threshold, the presence of finite-size particles can enhance the mean secondary flow and lead to particle accumulation in duct corners. Conversely, above this value, the strength of the secondary flow is reduced and particles are more likely to concentrate in the duct core regions. In addition, it was also found that inter-particle collisions play an important role in the near-wall particle distribution in closed duct flows, and their effect on particle diffusion in the duct cross-section is synergistic with that of the cross-sectional secondary flow [53]. Nonetheless, it is important to note that the topology and strength of the secondary flows in the open square duct flow investigated herein are distinctly different from those in closed duct flows, particularly near the upper corners of the mixed boundaries. Therefore, further investigations primarily aimed at elucidating the flow and particle dynamic modifications caused by the presence of high concentrations of inertial particles in turbulent open duct flows will be conducted in the near future.

Acknowledgments

This work is funded by the Natural Science Basic Research Program of Shaanxi Province (2023-JC-QN-0386), the Natural Science Research Program of Shaanxi Provincial Department of Education (22JK0621), and the Science Foundation of Yan'an University (YDBK2021-10). The authors also acknowledge the financial support from the Young Talent Fund of Association for Science and Technology in Yan'an, China, the Natural Science Basic Research Project of Shaanxi Province (2024JC-YBMS-252), the Shaanxi Provincial Administration for Market Regulation Science and Technology Project(2023KY23), and the Unveiling and Leading Projects of Yan'an University Natural Science Foundation (2023JBZR-019).

References

- [1] L. Chen, Z. Sun, H. Ma, G. Pan, P. Li, K. Gao, Flow characteristics of pneumatic conveying of stiff shotcrete based on CFD-DEM method, *Powder Technol.* 397 (2022) 117109.
- [2] B. Considine, A. McNabola, P. Kumar, J. Gallagher, A numerical analysis of particulate matter control technology integrated with HVAC system inlet design and implications on energy consumption. *Build. Environ.* 211 (2022) 108726.
- [3] S. T. W. Kuruneru, E. Sauret, K. Vafai, S. C. Saha, Y. Gu, Analysis of particle-laden fluid flows, tortuosity and particle-fluid behaviour in metal foam heat exchangers, *Chem. Eng. Sci.* 172 (2017) 677-687.
- [4] Z. Huang, C. Wang, Y. Yang, J. Sun, J. Wang, Y. Yang, B. Du, Modelling of gas-liquid-solid distribution in the cocurrent three-phase moving bed, *Chem. Eng. J.* 455 (2023) 140733.
- [5] B. Vreman, B. J. Geurts, N. G. Deen, J. A. M. Kuipers, J. G. M. Kuerten, Two- and four-way coupled Euler–Lagrangian large-eddy simulation of turbulent particle-laden channel flow, *Flow Turbul. Combust.* 82 (2009) 47-71.
- [6] A. Soldati, C. Marchioli, Sediment transport in steady turbulent boundary layers: Potentials, limitations, and perspectives for Lagrangian tracking in DNS and LES, *Adv. Water Resour.* 48 (2012) 18-30.
- [7] N. Almohammed, M. Breuer, Modeling and simulation of agglomeration in turbulent particle-laden flows: A comparison between energy-based and momentum-based agglomeration models, *Powder Technol.* 294 (2016) 373-402.
- [8] F. Rousta, B. Lessani, G. Ahmadi, Particle dispersion and deposition in wall-bounded turbulent flow, *Int. J. Multiphase Flow* 158 (2023) 104307.
- [9] A. Arsalanloo, M. Abbasalizadeh, Numerical study on deposition of particles in a 90° bend in the presence of swirling flow using Eulerian-Lagrangian method, *Powder Technol.* 320 (2017) 285-294.
- [10] M. Liu, J. Yao, Y.-L. Zhao, The dispersion of particles in turbulent semi-circular duct flows, *Petrol. Sci.* 18 (2021) 1240-1255.
- [11] H. Grosshans, C. Bissinger, M. Calero, M. V. Papalexandris, The effect of electrostatic charges on particle-laden duct flows, *J. Fluid Mech.* 909 (2021) A21.
- [12] Y. Yan, Y. Zhao, J. Yao, C. H. Wang, Investigation of particle transport by a turbulent flow through a 90° bend pipe with electrostatic effects, *Powder Technol.* 394 (2021) 547-561.
- [13] D. J. Phares, G. Sharma, A DNS study of aerosol deposition in a turbulent square duct flow, *Aerosol Sci. Tech.* 40 (2006) 1016-1024.

- [14] C. M. Winkler, S. L. Rani, S. P. Vanka, A numerical study of particle wall-deposition in a turbulent square duct flow, *Powder Technol.* 170 (2006) 12-25.
- [15] M. Fairweather, J. Yao, Mechanisms of particle dispersion in a turbulent, square duct flow, *AIChE J.* 55 (2009) 1667-1679.
- [16] J. Yao, M. Fairweather, Particle deposition in turbulent duct flows, *Chem. Eng. Sci.* 84 (2012) 781-800.
- [17] A. Noorani, R. Vinuesa, L. Brandt, P. Schlatter, Aspect ratio effect on particle transport in turbulent duct flows, *Phys. Fluids* 28 (2016) 115103.
- [18] Y. Wang, M. Fairweather, L. F. Mortimer, Y. Zhao, J. Yao, Mechanisms of particle preferential concentration induced by secondary motions in a dilute turbulent square duct flow, *Phys. Fluids* 32 (2020) 123313.
- [19] Q. Wang, K. D. Squires, M. Chen, J. B. McLaughlin, On the role of the lift force in turbulence simulations of particle deposition, *Int. J. Multiphase Flow* 23 (1997) 749–763.
- [20] A. E. Amiri, S. K. Hannani, F. Mashayek, Large-eddy simulation of heavy-particle transport in turbulent channel flow, *Numer. Heat Transf., B* 50 (2006) 285–313.
- [21] C. Marchioli, M. Picciotto, A. Soldati, Influence of gravity and lift on particle velocity statistics and transfer rates in turbulent vertical channel flow, *Int. J. Multiphase Flow* 33 (2007) 227–251.
- [22] H. H. Shin, L. M. Portela, C.E. Schaerer, N. Mangiavacchi, Dynamics of suspended sediment transport: A direct numerical simulation study, *Int. J. Multiphase Flow* 155 (2022) 104165.
- [23] W. Gao, P. Shi, M. Parsani, P. Costa, On the relevance of lift force modelling in turbulent wall flows with small inertial particles, *J. Fluid Mech.* 988 (2024) A47.
- [24] V. Armenio, V. Fiorotto, The importance of the forces acting on particles in turbulent flows, *Phys. Fluids* 13 (2001) 2437-2440.
- [25] L. F. Mortimer, D. O. Njobuenwu, M. Fairweather, Near-wall dynamics of inertial particles in dilute turbulent channel flows, *Phys. Fluids* 31 (2019) 063302.
- [26] C. M. Winkler, S. L. Rani, Relative importance of the lift force on heavy particles due to turbulence driven secondary flows, *Powder Technol.* 190 (2009) 310-318.
- [27] J. Yao, Fairweather M. Inertial particle resuspension in a turbulent, square duct flow, *Phys. Fluids.* 22 (2010) 33303.
- [28] R. Broglia, A. Pascarelli, U. Piomelli, Large-eddy simulation of ducts with a free surface, *J. Fluid Mech.* 484 (2003) 223-253.

- [29] N. Nikitin, Turbulent secondary flows in channels with no-slip and shear-free boundaries, *J. Fluid Mech.* 917 (2021) A24.
- [30] M. Yu, D. Modesti, S. Pirozzoli, Direct numerical simulation of flow in open rectangular ducts, *J. Fluid Mech.* 977 (2023) A32.
- [31] S. Kundu, K. Ghoshal, Effects of secondary current and stratification on suspension concentration in an open channel flow, *Environ. Fluid Mech.* 14 (2014) 1357-1380.
- [32] Y. Wang, Y. Zhao, J. Yao, Particle dispersion in turbulent, square open duct flows of high Reynolds number, *Powder Technol.* 354 (2019) 92-107.
- [33] Y. Wang, L. F. Mortimer, M. Fairweather, W. Ma, Y. Zhen, Particle transport in turbulent square duct flows with a free surface, *Phys. Fluids* 36 (2024) 13340.
- [34] J. Brosda, M. Manhart, Numerical investigation of semi-filled-pipe flow, *J. Fluid Mech.* 932 (2022) A25.
- [35] S. Komori, R. Nagaosa, Y. Murakami, S. Chiba, K. Ishii, K. Kuwahara, Direct numerical simulation of three-dimensional open-channel flow with zero-shear gas-liquid interface, *Phys. Fluids A* 5 (1993) 115-125.
- [36] P. F. Fischer, J. W. Lottes, S. G. Kerkemeier, NEK5000: Open source spectral element CFD solver, Available at: <http://nek5000.mes.anl.gov>, 2008.
- [37] A. T. Patera, A spectral element method for fluid dynamics: laminar flow in a channel expansion, *J. Comput. Phys.* 54 (1984) 468-488.
- [38] A. Noorani, G. Sardina, L. Brandt, P. Schlatter, Particle transport in turbulent curved pipe flow, *J. Fluid Mech.* 793 (2016) 248-279.
- [39] P. Bagchi, S. Balachandar, Effect of turbulence on the drag and lift of a particle, *Phys. Fluids* 15 (2003) 3496-3513.
- [40] L. Zeng, F. Najjar, S. Balachandar, P. Fischer, Forces on a finite-sized particle located close to a wall in a linear shear flow, *Phys. Fluids* 21 (2009) 033302.
- [41] J. Pantaleone, J. Messer, The added mass of a spherical projectile, *Am. J. Phys.* 79 (2011) 1202.
- [42] A. Huser, S. Biringen, Direct numerical simulation of turbulent flow in a square duct, *J. Fluid Mech.* 257 (1993) 65-95.
- [43] I. Nezu, Open-Channel Flow Turbulence and Its Research Prospect in the 21st Century, *J. Hydraul. Eng.* 131 (2005) 229-246.
- [44] S. Pirozzoli, D. Modesti, P. Orlandi, F. Grasso, Turbulence and secondary motions in square duct flow, *J. Fluid*

Mech. 840 (2018) 631-655.

- [45] Y. Joung, S.-U. Choi, Direct numerical simulation of low Reynolds number flows in an open-channel with sidewalls, *Int. J. Numer. Meth. Fluids* 62 (2010) 854–874.
- [46] S. Lovecchio, C. Marchioli, A. Soldati, Time persistence of floating-particle clusters in free-surface turbulence, *Phys. Rev. E* 88 (2013) 033003.
- [47] G. Sardina, P. Schlatter, L. Brandt, F. Picano, C M. Casciola, Wall accumulation and spatial localization in particle-laden wall flows, *J. Fluid Mech.* 699 (2012) 50-78.
- [48] A. Noorani, G. Sardina, L. Brandt, P. Schlatter, Particle velocity and acceleration in turbulent bent pipe flows, *Flow Turbul. Combust.* 95 (2015) 539-559.
- [49] R. Zamansky, I. Vinkovic, M. Gorokhovski, Acceleration statistics of solid particles in turbulent channel flow, *Phys. Fluids* 23 (2011) 113304.
- [50] S. Gerashchenko, N. Sharp, S. Neuscamman, Z. Warhaft, Lagrangian measurements of inertial particle accelerations in a turbulent boundary layer, *J. Fluid Mech.* 617 (2008) 255–281.
- [51] Z. Lin, Z. Yu, X. Shao, L.-P. Wang, Effects of finite-size neutrally buoyant particles on the turbulent flows in a square duct, *Phys. Fluids* 29 (2017) 103304.
- [52] W. Fornari, H. T. Kazerooni, J. Hussong, L. Brandt, Suspensions of finite-size neutrally buoyant spheres in turbulent duct flow, *J. Fluid Mech.* 851 (2018) 148-186.
- [53] H. Zhang, F. X. Trias, A. Gorobets, A. Oliva, D. Yang, Effect of collisions on the particle behavior in a turbulent square duct flow, *Powder Technol.* 269 (2015) 320-336.